UCRL-52568

A soft x-ray streak camera for laser fusion applications

Gary L. Stradling

(MS. Thesis)

April 1981

UCRL-52568

A soft x-ray streak camera for laser fusion applications

Gary L. Stradling

(MS. Thesis)

Manuscript date: April 1981

LAWRENCE LIVERMORE LABORATORY
University of California · Livermore, California · 94550

Available from : National Technical Information Service · U.S. Department of Commerce
5285 Port Royal Road · Springfield, VA 22161 · $8.00 per copy · (Microfiche $3.50)

A SOFT X-RAY STREAK CAMERA FOR LASER FUSION APPLICATIONS

A Thesis

Presented to the

Department of Physics and Astronomy

Brigham Young University

In Partial Fulfillment

of the Requirements for the Degree

Master of Science

by

Gary L. Stradling

April 1981

This Thesis, by Gary L. Stradling, is accepted in its present form by the Department of Physics and Astronomy of Brigham Young University as satisfying the thesis requirement for the degree of Master of Science.

Larry V. Knight, Committee Chairman

James M. Thorne, Committee Member

Dec 21, 1981
Date

Clark. G. Christensen, Graduate Coordinator

TABLE OF CONTENTS

LIST OF FIGURES

Chapter 1

INTRODUCTION

There is a well-justified concern about future supplies of energy. This concern extends beyond the question of potential energy sources and their availability. Problems of environmental degradation, waste disposal, nuclear fuel control, and political economics complicate the issue.

One potential energy source is controlled fusion. Fusion energy is widely acclaimed as a solution to several significant problems by virtue of the fuel availability and its relative cleanliness as an energy source. Although fusion energy production is not currently feasible, there is a concentrated research effort now underway in this country, the Soviet Union, Great Britain, France, Japan and other countries to prove that controlled fusion can be made feasible and to produce a fusion power plant.

Efforts are directed along two different approaches to controlled fusion. One approach is to magnetically confine a hot plasma for a sufficiently long time to produce fusion energy. The other approach is to compress and heat fusion fuel in a sufficiently short time that the inertia of the material confines the reaction at a density high enough for efficient fusion energy production. This approach is called inertial confinement fusion (ICF). Both the magnetic confinement and inertial confinement approaches are in early developmental stages.

This thesis will discuss the soft x-ray streak camera, an instrument developed to provide unique diagnostic coverage of inertial confinement fusion experiments. The design and applications of the soft x-ray streak camera will be presented in the context of inertial confinement fusion development. Specifically, the current requirements of the Laser Fusion Program at Lawrence Livermore National Laboratory (LLNL) will be considered.

Inertial Confinement Fusion

The processes which take place in inertial confinement fusion occur in very small volumes, last very short times, and involve enormous energy densities and mass compressions.

The actual scheme for producing ICF is to use a high-intensity energy source or "driver" to uniformly irradiate a small spherical pellet (target) containing fusion fuel (Fig. 1). A thin layer of the pellet surface is heated, causing material to ablate outward with high velocities. This ablating material, like the high-speed exhaust of a rocket, produces a reaction force which drives the pellet wall inward.[1] A shock wave is produced which converges at the target center. If the shock converges with sufficient uniformity and power, the fuel can be compressed and heated to thermonuclear ignition conditions.[2] A burn front, fed by alpha-particle capture, propagates

---

[1] J. Nuckolls, L. Wood, A. Thiessen and G. Zimmerman, Nature, Vol. 239, 139(1972); P. M. Campbell, G. Charatis, and G. R. Montry, Phys. Rev. Lett., Vol. 34, 74(1975).

[2] J. Nuckolls, J. Emmett and L. Wood, Phys. Today, Vol. 26, 46(1973); J. Emmett, J. Nuckolls and L. Wood, Sci. Am., Vol. 230, 24(1974).

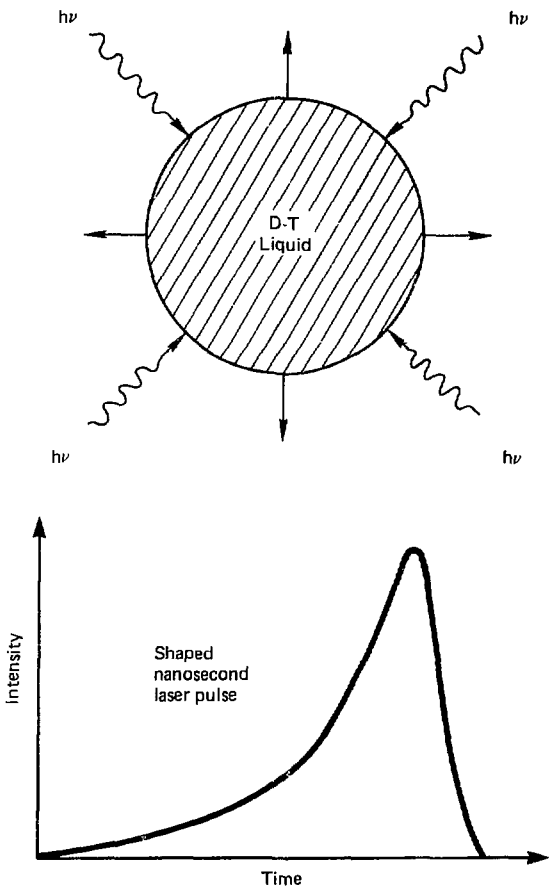

Figure 1. ICF scheme: the proposed target and the shape of the required driver pulse train.

outward from this ignition region at the target center, burning through the remaining fuel. In a successful reactor more energy must be released than was invested in the target compression.

This particular scheme has two major problems that must be overcome.[3] First, in order for the necessary compression to take place, the shock wave must converge uniformly over the surface of the ignition region. The compression process, however, has inherent Rayleigh-Taylor instabilities which result in small non-uniformities rapidly growing to significant proportions. The second major problem is that the target may undergo heating from high-energy electrons prior to the convergence of the shock wave. Any preheating of the fuel makes compression more difficult.

The delivery of sufficient energy at the required rate into a thin layer of the fuel pellet surface is a difficult task. A coronal plasma is formed as the pellet surface is heated. The absorption of energy in this plasma and the transport of energy to the pellet surface are dependent on a wide variety of plasma processes. The dominance of particular plasma processes in turn depends strongly on basic driver parameters.

To drive the pellet to a high enough gain for net energy production,[4] the energy source must deliver on the order of $\sim 10^6$ joules at the rate of $\sim 10^{14}$ watts, depending on the pellet design. This energy must be deposited uniformly over the very small

[3] D. T. Attwood, IEEE J. Quantum Electron., Vol. QE-14, 909(1978).

[4] J. H. Nuckolls, in Laser Program Annual Report-1979, edited by Lamar W. Coleman and John R. Strack, (Lawrence Livermore National Laboratory, 1980, UCRL-50021-79), Vol. 2, p. 3-2.

pellet surface. To be economically feasible the driver must be able to convert electrical energy to driving energy with 1-6-percent (wallplug) efficiency and be able to operate with a repetition rate of 4-8 Hz.

Focusable, high-power, pulsed energy sources such as lasers and ion beam devices[5] are the favored candidates for ICF powerplant drivers. Neither of these potential drivers, however, are at a level of development necessary to satisfy stringent powerplant requirements. Ion beam devices show considerable potential at this time. These types of machines currently operate with wallplug efficiencies of 25 percent. There are ion beam generators in development which have projected repetition rates as high as 10 Hz. High-power state-of-the-art lasers, which currently serve as the ICF development workhorses (such as the large Argus and Shiva lasers at LLNL) operate with power levels of 4 to 30 terawatts (TW). At best, this is only one percent of the power required for efficient energy production.

A significant increase in the understanding of inertial confinement fusion phenomena, as well as much technological development, is clearly necessary before ICF power plants can become a reality.

Laser Fusion

Although a powerplant-quality ICF "driver" has not yet been developed, currently available lasers are being used to explore ICF implosion dynamics. Laser fusion experiments, designed to demonstrate

---

[5]G. Yonas, Sci. Am., Vol. 239, 50(1978); S. G. Varnado, J. L. Mitchiner, unpublished, SAND-77-0516, Sandia Laboratories, 1977.

high compression, use a high-energy pulse of coherent light to drive the fuel pellet. This laser pulse delivers up to 10 kilojoules of energy to the pellet and lasts only a few hundred picoseconds (psec). The pellet implosion occurs on this same time scale. Typical laser fusion targets currently have diameters of about 100 microns.

The present glass laser systems are extremely inefficient. Nd:glass lasers have wallplug efficiencies of only 0.1 percent, and thus are designed for proof-of-principle experiments only. Some gas lasers, such as CO_2 lasers, can operate at high repetition rates and have wallplug efficiencies of as much as a few percent. The 10.6-micron CO_2 laser has its own problems, however.

Recent experiments have demonstrated that laser drivers with wavelengths longer than a fraction of a micron deposit significant amounts of the incident energy into penetrating, high-energy electrons.[6] Penetration by these high-energy electrons degrades the ablative performance of laser fusion targets. These and other experimental results point to the need for sub-micron wavelength lasers to drive sucessful target compression experiments.[7] High-power 0.53-μm wavelength lasers are currently being implemented at LLNL.

Laser Fusion Diagnostics

High-intensity laser light can interact with the plasma corona surrounding the pellet in a number of ways. Dominance of any of the

---

[6]R. E. Kidder, Bull. Am. Phys. Soc., Vol. 24, 925(1979); E. M. Campbell, V. C. Rupert, W. C. Mead, R. E. Turner, C. E. Max, K. G. Estabrook, F. Ze, Bull. Am. Phys. Soc., Vol. 25, 895(1980).

[7]C. Garban-Labaune, E. Fabre, and C. Max, Bull. Am. Phys. Soc., Vol. 25, 894(1980); E. M. Campbell (private communication).

available absorption and scattering processes depend on the laser wavelength, intensity, pulse duration, and the polarization of the incident field. Significant variations in the fraction of incident energy absorbed, in the velocity distribution of the heated plasma, and in the transport of that energy to the target surface result from changes in incident laser parameters. These quantities in turn affect the target implosion.

Information about the laser-plasma interaction phenomena and the pellet implosion process is contained in the radiation emission from the irradiated target. The types of radiation, its energy spectrum, the emission history, the source distribution, and the angular emission distribution are all signatures of the physical processes which occur in the experiment. If these observables are well diagnosed, comparison with the predictions of theoretical and computational modeling of the target dynamics can improve the understanding of the experiment and thus aid in designing pellets and drivers for higher compression and net energy production. For this reason a significant portion of the laser fusion effort is devoted to the development of diagnostic instruments capable of well-resolved temporal, spectral, and spatial measurements.

Expected emissions from the imploding target are scattered laser light and large quantities of x rays with spectra characteristic of plasma temperatures ranging from one hundred eV to several keV, as well as neutron and alpha particle reaction products.

Optical Measurements

Incident laser light is scattered by the coronal plasma through a variety of nonlinear plasma processes as well as by

reflection from the critical density surface. (Light will not *propagate in electron densities greater than the critical density*, which is a function of the signal frequency.) The ratio of the total energy in scattered light to the incident laser pulse energy gives the absorption efficiency at the target. Time integrated measurements of these quantities are made with optical calorimeters. The directional distribution of the scattered light is collected by photocells arrayed around the target. Optical spectrometers measure spectral shifts in the scattered light. This shift from the incident frequency is characteristic of non-linear scattering from the plasma as well as Doppler shifting of the scattered light.[8] The incident laser pulse is routinely characterized in terms of beam uniformity and temporal pulse shape.

X-Ray Diagnostics

The rate of x-ray emission from a plasma depends strongly on the temperature and density of the emitting material. In laser-plasma experiments there is a narrow region of moderate temperature and density where the rapidly falling density profile and the sharply rising temperature intersect.[9] This thin region between the ablation surface and the critical density surface emits radiation at a much higher rate than the cooler, denser, interior regions or the hot nebulous corona. The thermal x-ray emission spectrum of the target is

[8]D. Phillion, W. L. Kruer, and V. C. Rupert, Phys. Rev. Lett., Vol. 39, 1529(1977).

[9]M. D. Rosen, D. W. Phillion, V. C. Rupert, W. C. Mead, W. L. Kruer, J. J. Thomson, H. N. Kornblum, V. W. Slivinsky, G. J. Caporaso, M. J. Boyle, and K. G. Tirsell, Phys. Fluids, Vol. 22, *2020(1979)*.

thus a signature of the plasma density and temperature near the ablation surface. The evolution of that spectrum with time is characteristic of the heating and cooling processes of the system. These include heating by the laser pulse, cooling due to hydrodynamic expansion and radiation losses, and the rate of energy transport through the plasma to the target surface. The spatial distribution of the x-ray emission region reveals the uniformity of energy deposition and the symmetry of the implosion process. The rate of convergence of the emission region gives the implosion velocity.

X-ray emission spectra are obtained with grazing-incidence grating spectrometers, crystal spectrometers, and absorption-edge filtered x-ray diodes. The thermal x-ray spectrum ranges from 100 eV to 10 keV. Higher energy x rays are bremsstrahlung and photoionization products of fast electrons from the nonlinear plasma processes. The quantity, spectrum, and angular distribution of the high-energy x-ray tail can provide insight into hot electron production. X-ray microscopes using grazing-angle optics provide spatial and limited spectral data.[10]

Time-resolved x-ray spectral measurements are made using the LLNL ultrafast x-ray streak cameras which have a resolution limit of 15 psec.[11] Here, as with the x-ray diodes, spectral channels above a kilovolt are defined by absorption-edge filters and by a falling emission spectrum and decreasing detector response. A number of

---

[10]F. Seward, J. Dent, M. Boyle, L. Koppel, T. Harper, P. Stoering, and A. Toor, Rev. Sci. Instrum., Vol. 47, 464(1976).

[11]C. F. McConaghy and L. W. Coleman, Appl. Phys. Lett., Vol. 25, 266(1974); D. T. Attwood, L. W. Coleman, J. T. Larsen, and E. K. Storm, Phys. Rev. Lett., Vol. 37, 499(1976).

spectral channels are obtained by positioning different filters at several positions across the photocathode slit.

X-ray streak camera and x-ray microscope data can be correlated to yield the implosion time, the average implosion velocity, and the spectral emission from the target as a function of time. When coupled to a suitable imaging device, the x-ray streak camera's photocathode slit combines one-dimensional spatial resolution on the order of 5 microns with the usual 15-psec temporal resolution. Compression-front velocity and acceleration are extracted from this spatially and temporally resolved implosion data.[12]

Neutrons and Alpha Particles

Detection of reaction products is a measure of the success of thermonuclear reaction production. Neutron detectors measure the number of neutrons radiated, or the neutron yield. A neutron time-of-flight detector measures the neutron energy spectrum. The burn temperature can then be deduced from this energy distribution.[13] The burn region of high-energy implosions, where many energetic alpha particles escape the compression region, can be imaged using alpha-particle zone-plate-coded-imaging techniques.[14] This diagnostic can determine the size and shape of the thermonuclear burn region.

---

[12]D. T. Attwood, L. W. Coleman, M. J. Boyle, J. T. Larsen, D. W. Phillion, and K. R. Manes, Phys. Rev. Lett., Vol. 38, 282(1977); D. T. Attwood, B. W. Weinstein, and R. F. Huerker, Appl. Opt., Vol. 16, 1253(1977).

[13]R. A. Lerche, L. W. Coleman, J. W. Houghton, D. R. Speck, and E. K. Storm, Appl. Phys. Lett., Vol. 31, 645(1977).

[14]N. M. Ceglio and L. W. Coleman, Phys. Rev. Lett., Vol. 39, 20(1977).

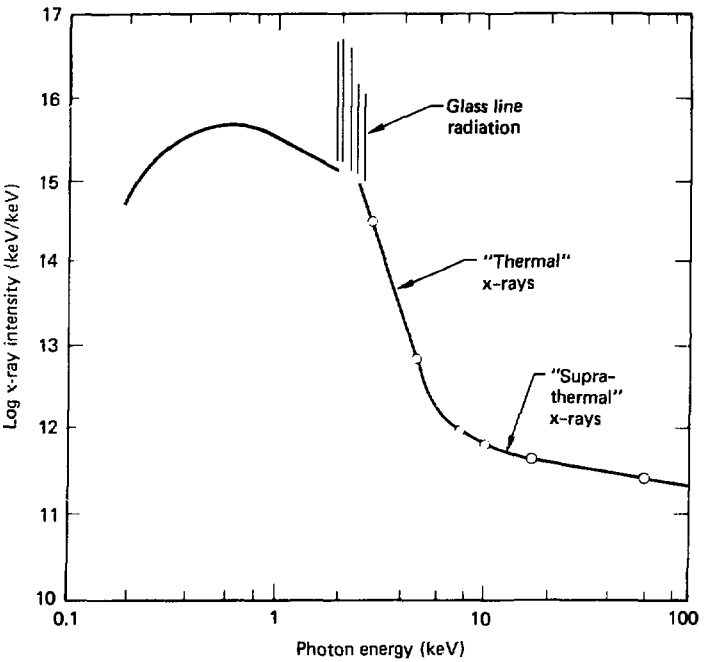

Figure 2. The x-ray emission spectrum from a glass-ball target shot.

Subkilovolt X-Ray Diagnostics

The time-integrated x-ray spectrum produced by a typical glass microsphere implosion is shown in figure 2. The x-ray diagnostics systems mentioned above are routinely able to temporally, spatially, and spectrally resolve superkilovolt x-ray emissions. However, for temperatures in the emission region of the plasma corona of 100 eV to 300 eV, there is a significant fraction of total x-ray flux in the subkilovolt region where detection is more difficult. These data are important to complete the energy balance and to help fill out the understanding of energy transport and implosion processes.

DANTE Subkilovolt Detectors

Windowless x-ray diode (XRD) detector systems called DANTE are used to measure subkilovolt x-ray emissions from target implosions. These x-ray diodes are absolutely calibrated for spectral response. The DANTE spectral resolution is provided by absorption edge filtering and by a detector response which falls with increasing energies. The spectral shape is deduced with subtraction unfolding techniques which compare a number of filtered channels. In some cases channel energy resolution is enhanced with x-ray reflectors. When combined with fast oscilloscopes, the x-ray diodes provide temporal resolution approaching 200 psec, and have a dynamic range of about ten.[15]

---

[15]H. N. Kornblum, L. N. Koppel, V. W. Slivinsky, S. S. Glaros, H. G. Ahlstrom, and J. T. Larsen, Bull. Am. Phys. Soc., Vol. 22, 1195(1977).

The Soft X-Ray Streak Camera

X-ray streak cameras routinely measure x-ray emissions above 1 keV with 15-psec temporal resolution, with broadband spectral discrimination, and with large dynamic range. Full diagnostic coverage of laser fusion experiments requires similar resolution of subkilovolt x-rays. The soft x-ray streak camera has been developed to supply that diagnostic capability. The soft x-ray streak camera (SXRSC) uses the same electron tube technology as optical and x-ray streak cameras but has an enlarged sensitivity range from 100 eV to 30 keV with improved spectral discrimination. A thin carbon window which transmits low-energy x rays is used as a photocathode substrate. The vacuum environment required for electron tube operation is supplied with a differential pumping system. The spectral discrimination is enhanced by grazing angle x-ray mirrors used with x-ray absorption filters for suppression of high-energy x-ray background. The SXRSC currently has three spectral channels with resolution $E/\Delta E \approx 3\text{-}6$.

This thesis introduces the soft x-ray streak camera and discusses its development, calibration, and experimental applications. In particular, the design criteria and the solutions to design problems are given. The problems considered are; detection of low-energy x-rays, vacuum compatibility, and spectral discrimination. Dynamic range and sweep calibration data are presented. Data from the high-power, Argus laser irradiation of a gold-disk are also given. Future work using the soft x-ray streak camera is discussed.

Chapter 2

SOFT X-RAY STREAK CAMERA DESIGN

The soft x-ray streak camera (SXRSC) is a modification[1] of the existing LLNL x-ray streak camera package.[2] The goal of the soft x-ray streak camera design is to provide acceptable sensitivity to x rays with energies between 100 and 1000 electron volts. To utilize existing technology the SXRSC must conform to certain x-ray streak camera specifications. The commercially available image converter tube[3] and the existing LLNL electronics and chassis design have been retained with only minor alterations. Major changes were made to the camera front end including the cathode assembly and the high-voltage standoff design, as well as the addition of a differential vacuum-pumping system and reflector-filter spectral discriminator.

The X-Ray Streak Camera

In order to give a clear description of the soft x-ray streak camera, the basics of the LLNL x-ray streak camera operation and

---

[1]G. L. Stradling, D. T. Attwood, J. W. Houghton, E. L. Pierce, and D. P. Gaines, Bull. Am. Phys. Soc., Vol. 23, 880(1978).

[2]C. F. McConaghy and L. W. Coleman, Appl. Phys. Lett., Vol. 25, 268(1974).

[3]The cathodeless image converter tube used is manufactured by RCA, model number C73435A(Blank); RCA Electronic Components, C73435 series, data sheet 7-72, Harrison, N. J., 1972; R. G. Stoudenheimer, unpublished, RCA Image Tube Application Note, AN-4789, RCA Electronic Components, October 1971.

design will be discussed here. X-ray emission from the target arrives at the camera shortly after an optical trigger signal from the laser. As the optical trigger pulse initiates the breakdown of an avalanche-transistor circuit, the x-ray signal reaches the photocathode, ejecting electron current into the image converter tube. The image converter tube translates this temporally-varying electron emission into a spatially-modulated, streaked image on a fluorescent screen. The image is amplified to photographable intensities with a 40-mm diameter microchannel-plate image intensifier. The temporal resolution limit of the x-ray streak camera is 15 psec, and for most laser fusion applications it has a dynamic range greater than one thousand. Figure 3 is a schematic of basic x-ray streak camera operation.

The Image Converter Tube

The image converter tube (ICT), the central component of the streak camera, converts the incident x-ray signal into an electron current which is electrically focused and streaked before being reconverted into an optical image on a fluorescent screen. X rays are incident on the front of a thin slit-shaped transmission photocathode, producing an emission current of slow electrons from the back surface proportional to the incident flux. These electrons are accelerated to 2.5 keV by an acceleration grid, pass through a focusing field and continue to be accelerated to 17 keV. The focusing optics image the slit-shaped electron-emission region of the photocathode onto an optical phosphor. This stream of electrons passes between a pair of deflection plates positioned after the focusing optics. A rapidly changing electric field between the deflection plates sweeps the

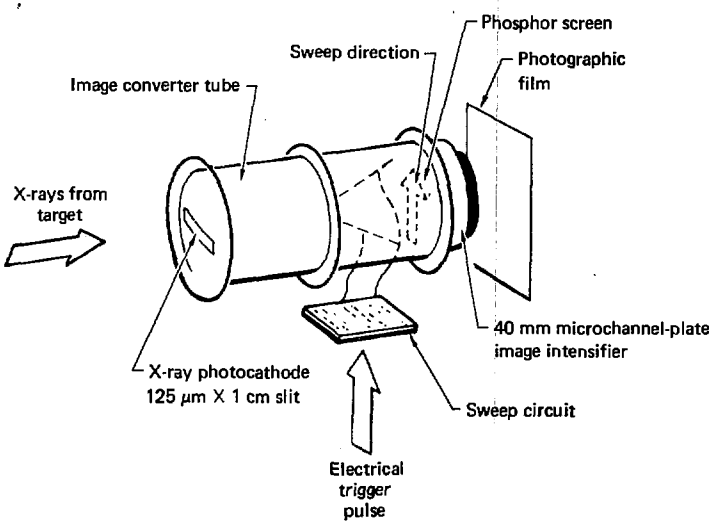

Figure 3. Streak camera operation schematic. X rays are incident on the photocathode a few nanoseconds after an electric trigger pulse arrives at the avalanche transistor sweep circuit. Electrons from the photocathode are imaged on the phosphor and swept with time to provide x-ray intensity-versus-time information.

electron current perpendicular to the slit direction, streaking the image in time. The resulting data streak retains spatial information of the photocathode emission along the slit dimension and exhibits the temporal modulation of the incident x-ray signal in the time direction.

The image converter tube is shown in figures 4 and 5. Figure 4 is a radiograph of the ICT showing the actual configuration of the electron-focusing geometry. Figure 5 identifies the photocathode (-17 kV), acceleration grid (-14.5 kV), focusing cone (-16.2 kV), anode (ground potential), deflecting electrodes, fluorescent screen and fiberoptic coupler. Also shown in figure 5 is the microchannel-plate image intensifier as it is oriented on the ICT.

The Photocathode and Photocathode Substrate

The x-ray streak camera photocathode generally consists of a ~100-Å gold layer deposited on a transmission substrate. The photocathode aperture is defined by a slit nominally 125 μm wide and 13 mm long. Because the ICT operates at a vacuum approaching 10^{-6} Torr, the photocathode substrate has also served as a barrier against atmospheric pressure. The standard, suprakilovolt x-ray streak camera uses an eight-micron-thick beryllium foil as a photocathode substrate and vacuum barrier. This substrate is strong enough to withstand atmospheric pressure, but exhibits high absorption of subkilovolt x rays (Fig. 6), introducing a one kilovolt low-energy cutoff in the camera sensitivity.

X rays which are transmitted through the substrate layer, and which are absorbed in the photocathode, excite Auger- and

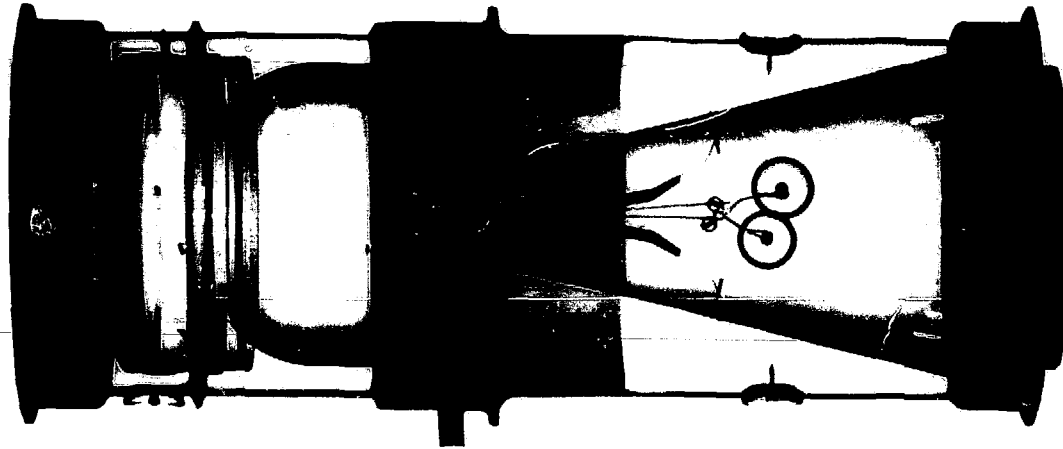

Figure 4. Radiograph of the RCA image converter tube, model number C73435A (Blank).

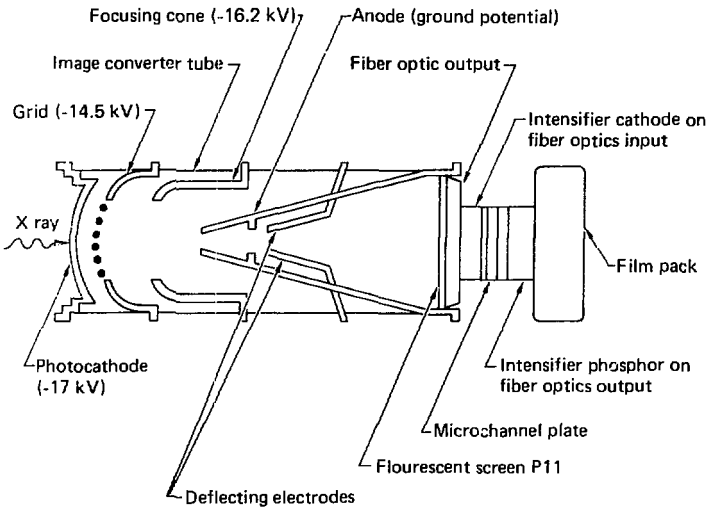

Figure 5. Image converter tube design schematic. X rays eject secondary electrons from the photocathode. The secondary electrons are accelerated to the grid, imaged by the focusing cone, and then swept across the P11 fluorescent screen. The image on the phosphor is amplified by the image intensifier and then recorded on photographic film.

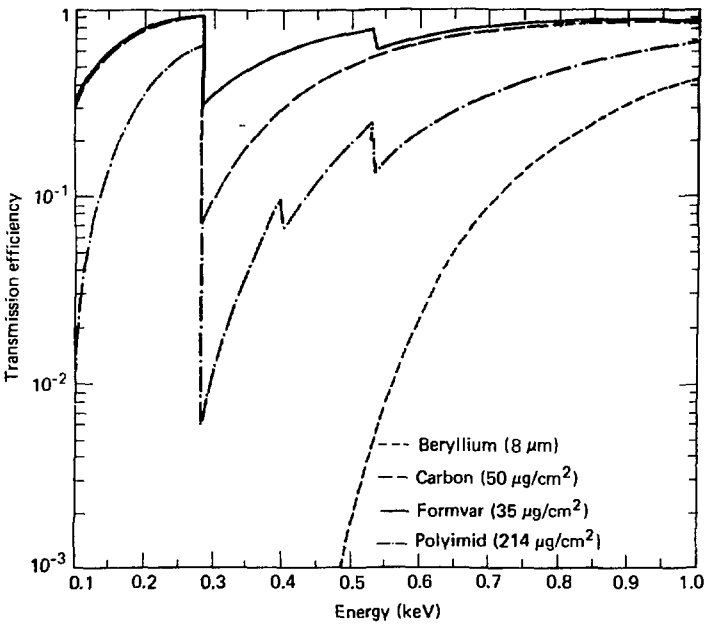

Figure 6. X-ray transmission efficiencies for 8-μm beryllium, 50-$\mu g/cm^2$ carbon, 35-$\mu g/cm^2$ formvar, and for 215-$\mu g/cm^2$ polyimid.

photo-electrons. These fast primary electrons give up energy in the photocathode through collisional excitation of secondary-electron cascades.[4] Those electrons which reach the photocathode boundary with sufficient perpendicular velocity to surmount the surface energy barrier are ejected as cathode current. This current is composed mainly of a secondary-electron distribution with energies of a few electron volts and a much smaller quantity of high-energy primary electrons.

Photocathode conversion efficiency is optimized by a low work function and by long secondary-electron mean free paths which result in a maximum emission depth of electrons in the photocathode. The optimum photocathode thickness for x ray-to-electron conversion (where the x-ray mean free path is much larger than that of the electrons) is then the secondary-electron emission depth.

The Image Intensifier

The 40-mm microchannel-plate image intensifier is shown schematically in figure 7. This type of intensifier is a very compact, relatively distortion-free photomultiplier device. Photons from the streaked image on the ICT phosphor eject electrons from the intensifier photocathode. These electrons are then accelerated along many very narrow glass-walled channels. As they impact the lead-rich walls of the channels, they produce cascades of other electrons. The much amplified group of electrons then strikes a phosphor, producing a visible image of photographable intensity.

---

[4]B. L. Henke, J. P. Knauer, and K. Premaratne, J. Appl. Phys. (to be published); B. L. Henke, J. A. Smith, D. T. Attwood, Appl. Phys. Lett., Vol. 29, 539(1976).

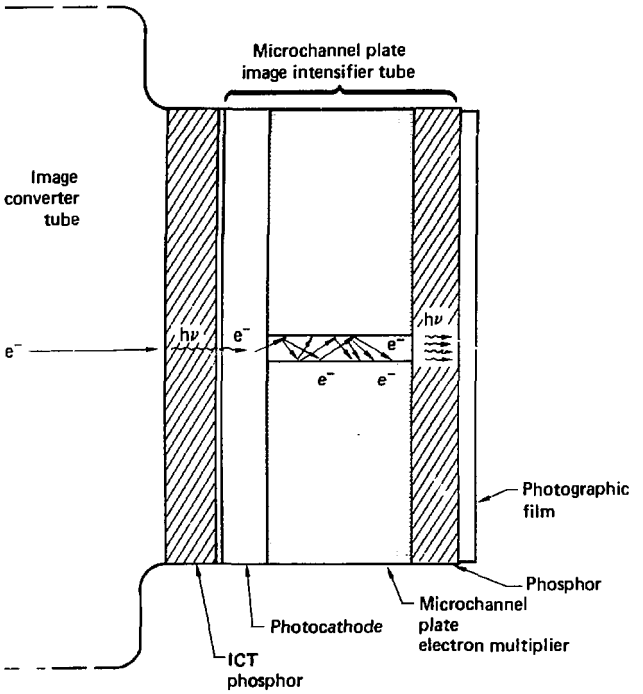

Figure 7. Microchannel-plate image intensifier design schematic. Photons eject electrons from the microchannel plate photocathode. These electrons are accelerated through very narrow lead-glass channels and produce cascades of electrons when they impact the high electron-density walls of the channels. This amplified electron signal strikes a fluorescent screen and produces an image of photographable intensity.

Temporal Resolution

The temporal detail resolvable by the streak camera is limited through the temporal and spatial blurring inherent in the individual signal transfer components of the camera. If the incident signal were a Gaussian in time and the individual resolution contributions were also Gaussian, we could calculate the total system resolution as the quadratic sum of the various resolution elements:

$$\tau_{tot} = (\Sigma_i \tau_i^2)^{1/2}, \qquad (1)$$

where τ_i are the contributions to the temporal resolution limit from the various camera components. Although the components of this resolution system will not likely be statistically independent Gaussians, this method of analysis can be used to give an estimate of the total system resolution.[5]

Temporal blurring results from transit time spreading during transport of the electron signal from the photocathode to the optical imaging phospher. An x-ray signal incident on the photocathode produces electron emission (mostly low-energy secondaries) with a distribution of energies. As these electrons are accelerated through the image converter tube to the imaging phosphor, there is a spread in transit times due to the spread in electron velocities.

---

[5]E. K. Zavoiskii and S. D. Fanchenko, Dok. Akad. Nauk. SSSR [Sov. Phys. Dokl.], Vol. 100, 661(1955); Dok. Akad. Nauk. SSSR [Sov. Phys. Dokl.], Vol. 108, 218(1956); Appl. Opt., Vol. 4, 1155(1965); D. J. Bradley, U. S. Patent No. 3 761 614(25 September, 1973); and with particular refrence to the LLNL optical streak cameras, J. W. Houghton, S. W. Thomas, L. W. Coleman, ISA Trans., Vol. 14, 196(1975).

This transit time spread is expressed as:[6]

$$\tau_1 = 2.34 \times 10^{-8} \frac{(\Delta\varepsilon)^{1/2}}{E} \text{ (sec)} \qquad (2)$$

Where $\Delta\varepsilon$ is the width of the electron energy distribution (eV) at the photocathode and E is the extraction field strength (V/cm). The energy distribution width of secondary electron emission due to subkeV x-ray illumination of a gold photocathode has been measured by Henke, *et. al.* (Ref. 4) to be 3.8 eV. The x-ray streak cameras operate with an extraction field of 2500 V across 4.2 mm. Thus, E is 5900 V/cm and τ_1 is 7.7 psec.

The remaining contributions to the overall temporal resolution are due to spatial resolution limitations of the finite photocathode slit width and the electron imaging system, coupled with the camera sweepspeed. The temporal resolution limit from the photocathode slit is the time required to sweep through the imaged slit width,

$$\tau_2 = rMd. \qquad (3)$$

For our system, the slit width d is 0.125 mm, the system magnification M is 1.35, and the inverse sweepspeed r of the fastest sweep circuit is 35 psec/mm. The resulting resolution contribution τ_2 is 5.9 psec.

The electron imaging resolution limit δ of the x-ray streak camera has been crudely measured to be ~10 line pairs/mm using a 100-μm wire mask. The temporal resolution limit due to the finite electron focusing capability of the system is then

[6]V. V. Korobkin, A. A. Malyutin, and M. Ya. Schelev, J. Photogr. Sci., Vol. 17, 179(1969).

$$\tau_3 = \frac{\nu M}{\delta}. \qquad (4)$$

Using the above values of ν, M, and δ, τ_3 is 4.7 psec. The total temporal resolution τ_{tot} of the system can then be estimated by equation 1 to be ~11 psec.

A direct measurement of the time resolution limit of the system is preferable to indirect calculations. A very short pulse, ~1-psec, x-ray source is not currently available, but measurements of 30-psec x-ray pulses are consistent with a value of τ_{tot} of 10-15 psec. The effect of a non-zero resolution limit on the measured signal can be roughly estimated with the Gaussian quadrature approximation used above. For example, a 100-psec signal detected with a 15-psec resolution system will be broadened by ~1 percent. X-ray-emission temporal detail on a scale relevent to laser fusion experiments (~100 psec) are thus well resolved with this conservative system resolution of 15 psec.

Subkilovolt X-Ray-Transmitting Cathode Substrate

The x-ray streak camera sensitivity can be extended below the 1-keV limit of the standard beryllium window by the substitution of a thinner and/or more transparent window.

X-Ray Absorption

X-ray absorption is a well-studied process. In the x-ray energy range of interest here, photoionization is the principal mechanism for absorption. The amount of attenuation experienced by x rays of intensity I_o traversing a material of thickness x and density ρ is described by

$$\frac{I}{I_o} = \exp(-\mu\rho x). \qquad (5)$$

The x-ray absorption coefficient μ is a function of the material and the x-ray energy. Sharp jumps in absorption coefficients are measured for energies near the excitation energies of electrons in the material. As an example of the sharpness and spacing of the absorption edges seen in all materials, figure 8 shows the energy dependence of the absorption coefficients[7] of tungsten for x-ray energies between 0.1 and 1000 kilovolts.

Substrate Selection

Figure 6 shows the expected transmission curves of several commercially available substrate materials and a comparison with the previously used 8-μm beryllium. Of these, 50-$\mu g/cm^2$ carbon and 35-$\mu g/cm^2$ Formvar offer the highest transmission of x rays with energies below 300 eV. Carbon also provides the sharpest high-energy cutoff at the carbon K-edge. We found 50-$\mu g/cm^2$ carbon foils to be readily available, unexpectedly durable, and convenient to work with. These foils have been used as photocathode substrates in SXRSC experiments to date. Other substrates can easily be implemented.

Vacuum System Design

The very thin foils needed for subkilovolt x-ray transmission are unable to withstand the pressure differential between atmospheric pressure and the vacuum level required for ICT operation. A vacuum

---

[7]W. H. McMaster, N. Kerr Del Grande, J. H. Mallett, and J. H. Hubbell, unpublished, UCRL-50174, Rev. I, Sec. II, Lawrence Livermore National Laboratory.

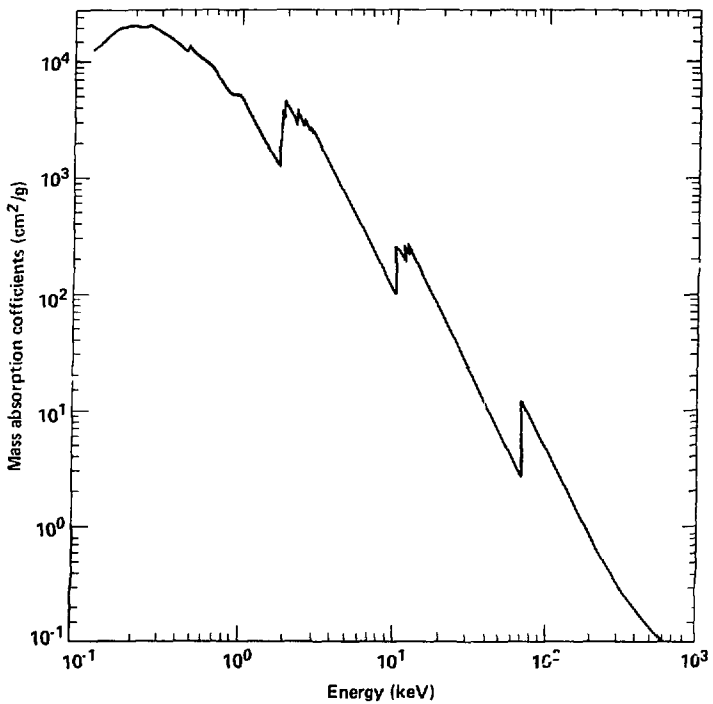

Figure 8. X-ray absorption coefficients for tungsten. The x-ray absorption coefficient increases sharply at the electron binding energy resonances, resulting in absorption edges in the material's transmission properties.

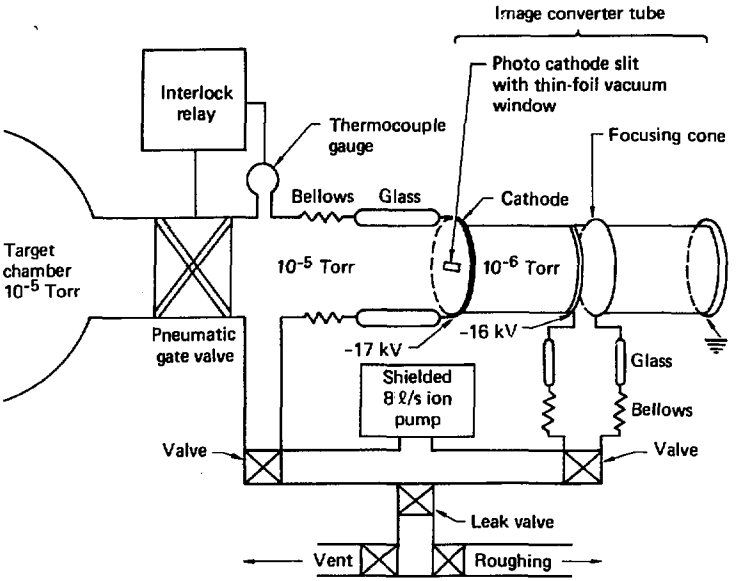

Figure 9. Differential vacuum-pumping system design schematic. The thin foil photocathode and substrate are protected from an excessive pressure differential by a differential pumping arrangement and a pressure interlock system. Glass connectors provide insulation between the ICT high-voltage regions and the pumping system.

system was designed (Fig. 9) to differentially pump across the photocathode substrate and to actively pump the image converter tube. This system eliminates pressures on the thin foil of greater than 10^{-3} Torr and allows a vacuum of 10^{-6} Torr to be maintained inside the ICT. The image converter tube is pumped through a pumpout tubulation located on the ICT focusing cone.

A pneumatic gate valve coupled with a thermocouple vacuum-gauge interlock relay provides partial protection to the photocathode against slow venting of the target chamber. The ICT is actively pumped by an eight-liter-per-second ion pump.[8]. The ion pump is shielded to limit external magnetic fields in the electron imaging region of the ICT. The vacuum region in front of the photocathode is maintained at about 10^{-5} Torr by the target chamber vacuum system. External roughing and venting are routed through a variable leak valve to insure slow variations in pressure. In spite of these precautions, convenient photocathode replacement is both prudent and desirable. The cathode cup assembly and the image converter tube front plate were redesigned to allow easy photocathode replacement and to accommodate the vacuum system geometry. The new cathode cup and ICT front face plate design maintain the standard x-ray streak camera cathode-to-acceleration-grid separation of 4.2 mm.

---

[8]Eight-liter-per-second Vac Ion Pump, Model 911-5005, manufactured by Varian Associates, Palo Alto, California.

Chapter 3

REFLECTOR-FILTER ENERGY CHANNEL DISCRIMINATORS: THEORY AND DESIGN

Broadband spectroscopy of subkilovolt x-ray emissions from laser-fusion experiments has neither of the advantages of a falling photocathode spectral response or of a *falling target emission* spectrum, both of which limit high-energy background in absorption-edge filtered suprakilovolt x-ray measurements. A gold photocathode has a relatively-flat response for photon energies between 100 and 1000 electron volts. The spectral emission of a glass ball target (shown in figure 2) does not begin to fall significantly until well into the suprakilovolt region. Simple absorption-edge filtering is insufficient to provide an unambiguous energy channel.

A well-known x-ray technique for obtaining a relatively-narrow broadband energy channel with a sharp high-energy cutoff is to combine a grazing-angle x-ray mirror with an absorption-edge filter (Fig. 10). The *rapidly falling filter transmission discriminates against* lower-energy x rays. The drop in x-ray mirror reflective efficiency above a high-cutoff energy E_c provides for the necessary supression of the high-energy component of the target emission spectrum. This chapter presents a simplified description of this phenomona in terms of atomic resonances.

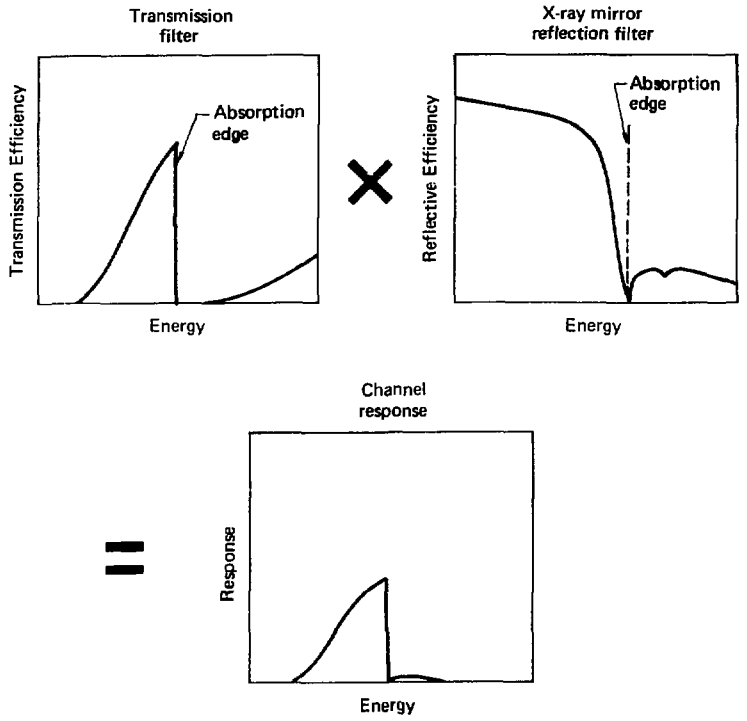

Figure 10. Reflector-filter channel discriminator design. The absorption edge of a transmission filter combined with the high-energy fall-off in reflectivity of an x-ray mirror provide a narrow spectral channel.

Grazing-Incidence X-Ray Reflection

Grazing angle x-ray reflection techniques make use of total external reflection phenomena. Total external reflection is observed when electromagnetic waves in a medium of refractive index n_1 are incident at appropriately large angles upon a medium of lower refractive index n_2 (Fig. 11). This phenomenon derives from the requirement that phases match at the boundary, as described by Snell's Law:

$$\frac{\sin\theta_1}{\sin\theta_2} = \frac{n_2}{n_1} \tag{6}$$

Considering x rays incident from a vacuum onto most common metals and many other materials, n_2 is slightly less than unity and $n_1 = 1$. The condition of total external reflection is that for n_2 less than unity, θ_1 is greater than some critical angle θ_c where

$$\theta_c = \sin^{-1} n_2. \tag{7}$$

Under this condition Snell's Law is not satisfied by any real angle θ_2, indicating that propagation within region 2 does not occur, and that total external reflection results.

To appreciate total reflectivity, it is instructive to consider the simplified model of atoms in medium 2 with a single resonance level E_o. In this approximation the index of refraction, n_2 satisfies[1]

[1]Arnold Sommerfeld, Optics (Academic Press Inc., New York, 1964), Chap. III, p. 97; Arthur H. Compton, Samuel K. Allison, X-Rays in Theory and Experiment (D. Van Nostrand Company, Inc., New Jersey, 1926), Chap. IV, p. 293.

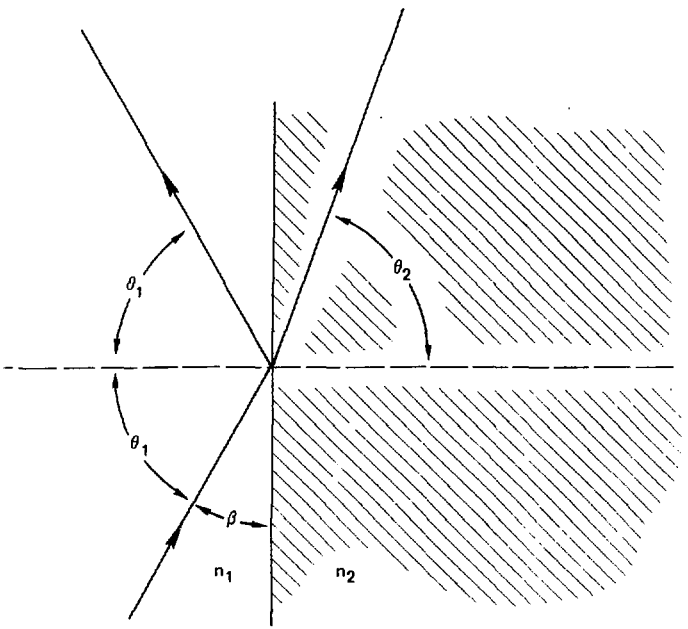

Figure 11. Reflection of electromagnetic waves at a plane interface.

$$n_2^2 = 1 + \frac{Ne^2\hbar^2/m\varepsilon_o}{E_o^2-E^2-igE_oE} \qquad (8)$$

where E is the x-ray energy, g is a damping factor, N is the number of dispersion electrons per unit volume, e is the electron charge, m is the electron mass, and ε_o is the permitivity of free space. For E much greater than E_o and for small loss terms, n_2^2 can be further approximated by

$$n_2^2 \approx 1 - \frac{Ne^2\hbar^2}{E^2m\varepsilon_o}, \qquad (9)$$

which is less than unity. In practice n_2 is a complicated quantity which involves a sum over all of the resonance levels of the atom. However, the rigorous, many-resonance treatment of x-ray reflection is beyond the scope of this description, and will not be presented here. The single resonance approximation illustrates the physical basis for total external reflection of x rays and its description will be followed by the more complete numerical modeling of others, as appropriate to the designs of this thesis.

To continue with the simplified model, the critical angle for reflection θ_c is seen to depend on x-ray energy. The definition of θ_c,

$$\sin\theta_c = n_2, \qquad (10)$$

and the approximation for n_2^2 in equation 9 gives

$$\sin^2\theta_c \approx 1 - \frac{Ne^2\hbar^2}{E^2m\varepsilon_o}. \qquad (11)$$

A trignometric identity converts this to

$$\cos^2\theta_c \approx \frac{Ne^2\hbar^2}{E^2m\varepsilon_o} \qquad (12)$$

or,

$$\cos\theta_c = \frac{E_p}{E}, \tag{13}$$

with E_p, the plasma "cutoff" energy, defined by

$$E_p = 3.72\text{x}10^{-14}N^{1/2}\ (\text{keV}). \tag{14}$$

The electron density in equation 14 is in units of e/cm^3. E_p is in keV. If the grazing angle β is defined as

$$\beta = 90 - \theta_1, \tag{15}$$

then

$$\cos\theta_1 = \sin\beta. \tag{16}$$

For most x-ray applications β is small enough that, to first order,

$$\sin\beta \approx \beta. \tag{17}$$

The critical grazing angle β_c is then defined as

$$\beta_c = \frac{E_p}{E} \tag{18}$$

For a given grazing angle β and for photon energies high enough that β_c is smaller than β, the reflection efficiency decreases and the propagation and the absorption of x rays in region 2 occurs. The reflection-efficiency-versus-energy response of an x-ray reflector at some grazing angle β therefore has a high-energy cutoff E_c, which depends on both the grazing angle and the electron density:

$$E_c = \frac{E_p(N)}{\beta}. \tag{19}$$

There is an atomic number (Z) dependence in the cutoff energy E_c from the $N^{1/2}$ term contained in E_p. The cutoff energy thus increases roughly as the square root of Z. $E_c(\beta)$ for gold would be

expected to be only a factor of 4.4 larger than the $E_c(\beta)$ for beryllium, in reasonable agreement with measurements.

The selection of reflectors with suitable high-energy x-ray suppression characteristics requires a more exact determination of the energy-dependent reflective efficiency than this model provides. A more complete calculation including all electronic resonances is necessary. The more thorough analysis shows that the sharpness of the energy cutoff decreases with the number of resonances present in the material.

A detailed computer code,[2] REFLECT2, was used to calculate x-ray mirror reflective-efficiency-versus-energy curves for various grazing angles. Using a semiclassical dispersion theory, this code calculates atomic scattering factors by an appropriate integration over photoionization cross sections which include all of the electronic resonances. REFLECT2 correlates well with empirical measurements except in energy regions near x-ray absorption edges of the material.

X-Ray Reflector-Filter Design

The three design parameters of an x-ray reflector, absorption-edge filter spectral-channel discrimination system are the absorption filter, the reflector material, and the grazing angle. The channel definition, particularly the low-energy cutoff, is determined

[2]A. Toor and H. F. Finn, computer code REFLECT2 (Lawrence Livermore National Laboratory, Livermore, Ca.). The photoionization cross sections for subkilovolt x rays used by this code are from B. L. Henke, University of Hawaii. The cross sections for higher energy x rays are from the LLNL cross section library file CSLOW3/77.

by the composition and thickness of the absorption filter. The position and effectiveness of the critical-energy cutoff are functions of the reflection angle and the Z of the x-ray mirror. Low-Z materials with few resonances exhibit the sharpest cutoffs. The high-energy cutoff can be optimized if the reflector and the absorption filter are both chosen to have an absorption edge near the desired cutoff energy, as in the reflector and absorber curves in figure 10.

Design of Three Specific Subkilovolt Energy Channels

An intermediate goal for SXRSC implementation has been to field the instrument on gold-disk target experiments at the Argus laser facility with three well-defined subkilovolt spectral channels:[3] the first below 300 eV, the second below 500 eV, and the third below 700 eV.

Absorption-edge filter materials with interesting edges in this region are carbon, titanium, vanadium, chromium, iron, and cobalt. Carbon, vanadium, and iron were selected as filters for the three channels because they have absorption edges at 283 eV, 513 eV, and 708 eV respectively, and because of their availability and their handling characteristics as thin foils.

Three mirrors were then selected for the sharpness of their reflectivity cutoffs near the absorption edges of the corresponding filters. Figures 12 and 13 show characteristic reflectance curves for both carbon and nickel at 2°, 3°, 4°, and at 5°. The three selected

[3]R. L. Kauffman, G. L. Stradling, and D. T. Attwood, Bull. Am. Phy. Soc. Vol. 23, 880(1978).

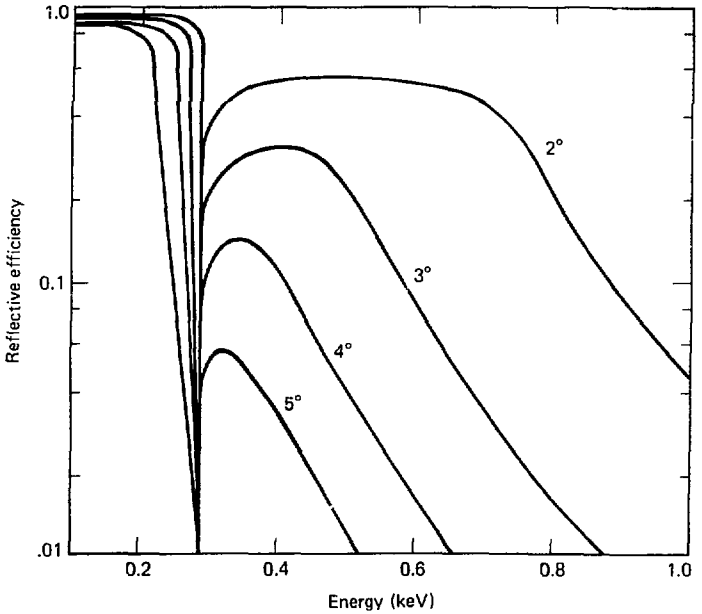

Figure 12. Carbon x-ray reflector efficiencies at 2°, 3°, 4°, and 5°.

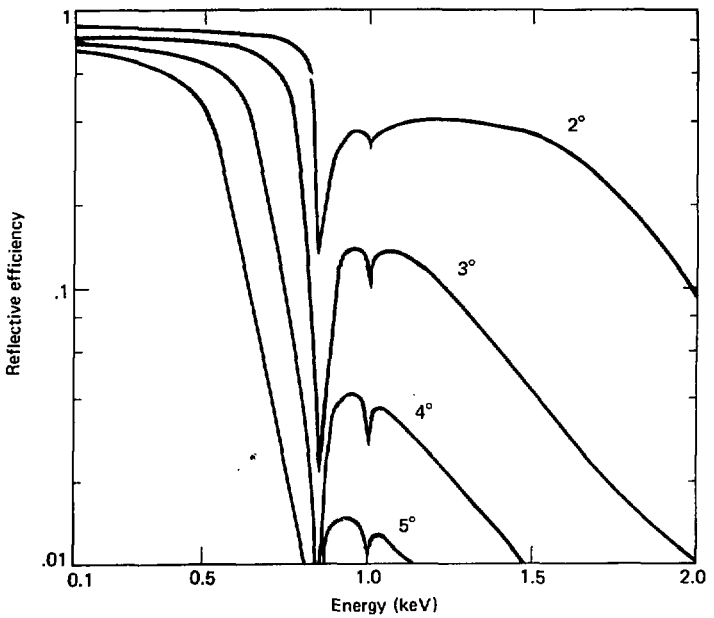

Figure 13. Nickel x-ray reflector efficiencies at 2°, 3°, 4°, and 5°.

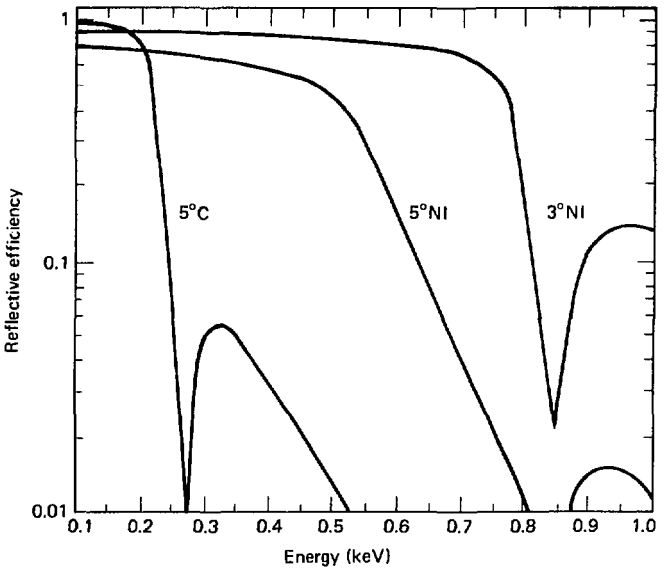

Figure 14. Efficiencies of three selected x-ray reflectors: carbon at 5°, nickel at 5°, and nickel at 3°.

reflector material-angle combinations are carbon at 5°, nickel at 5°, and nickel at 3° (Fig. 14). The reflective-efficiency of carbon at 5° falls off rapidly above the carbon edge. Nickel at 5° provides a cutoff at 600 eV. Nickel at 3° gives the high-energy cutoff at 800 eV.

The three energy channels were optimized to obtain nominally equal flux levels through each reflector-filter combination. The responses of each of the energy channels were calculated by folding together the contributions from the individual channel components: the reflective efficiency of the x-ray reflector, the transmission efficiency of the absorption-edge filter and of the carbon photocathode substrate, and the theoretical response of the gold photocathode. The flux level to be expected in each channel was then obtained by folding the channel spectral response with the emission spectrum anticipated from the target, and then integrating over the spectrum. The absorber filter thicknesses were chosen to set the channel responses at the desired level.

For irradiation of gold-disk targets the spectrum can be reasonably approximated by a 150-eV blackbody.[4] The response of the gold photocathode is roughly proportional to the product of the photon energy E and the energy-dependent absorption efficiency of the

[4]M. D. Rosen, D. W. Phillion, V. C. Rupert, W. C. Mead, W. L. Kruer, J. J. Thomson, H. N. Kornblum, V. W. Slivinsky, G. J. Caporaso, M. J. Boyl, and K. G. Tirsell, Phys. Fluids, Vol. 22, 2020(1979).

photocathode $\sim\mu(E)$. $E\mu(E)$ corresponds to the amount of energy deposited in the photocathode.[5]

The transmission curves of the filters and the photocathode substrate, and the absorption of the photocathode, are easily calculated from low-energy mass absorption cross sections compiled by Henke.[6] Figure 15 gives the combination of: an anticipated source spectrum from a gold-disk target; the theoretical $E\mu(E)$ cathode response for a 100-Å gold photocathode; the transmission efficiency for the 50-$\mu g/cm^2$ carbon substrate; the three x-ray mirror reflective efficiency curves; three selected filter transmission curves, and the folded combination of them all. A schematic showing the operational configuration of the three-channel reflector-filter system is shown in figure 16.

The five-degree maximum grazing angle for the mirrors requires that the SXRSC be oriented at 10 degrees to the radiated x rays. Mirror fine positioning is required in the θ, φ, and z directions. A housing was designed to position the three mirrors and to support the SXRSC at ten degrees with respect to the target chamber port. Figure 17 shows the SXRSC assembled with the x-ray mirror housing.

---

[5]B. L. Henke, J. P. Knauer, and K. Premaratne, J. Appl. Phys. (to be published); B. L. Henke, J. A. Smith, D. T. Attwood, Appl. Phys. Lett., Vol. 29, 539(1976).

[6]B. L. Henke and E. S. Ebisu, Advances in X-Ray Analysis, edited by C. L. Grant, C. S. Barrett, J. B. Newkirk, and C. O. Ruud (Plenum, New York, 1974), Vol. 17, pp. 150-213.

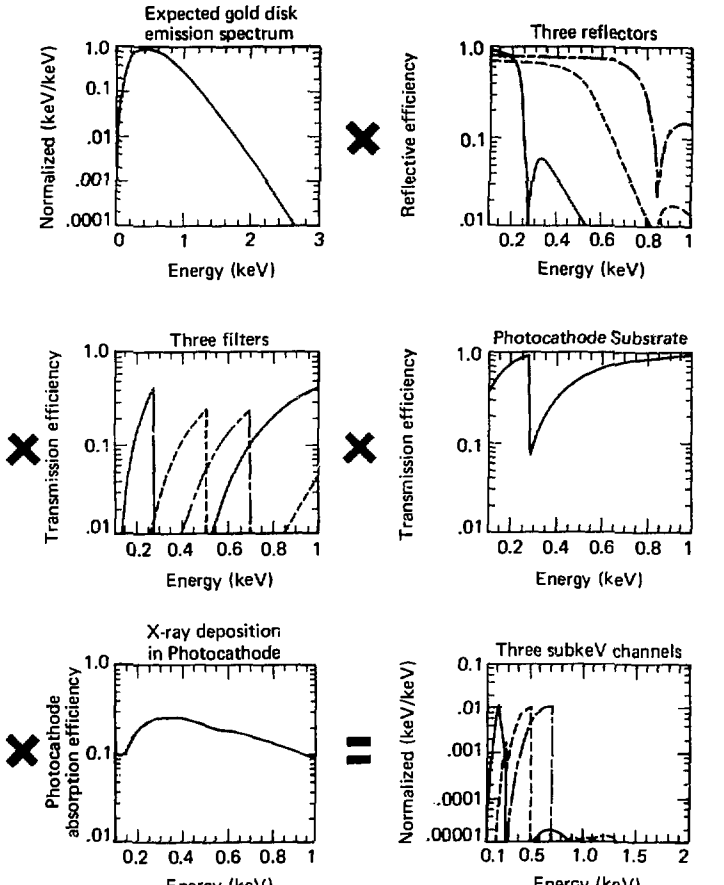

Figure 15. Three-channel reflector-filter design. The three broadband spectral channels are obtained by folding together the source spectrum, the x-ray mirrors' reflective efficiencies, the absorption filters' transmission efficiencies, the photocathode substrate's transmission efficiency, and the photocathode conversion efficiency.

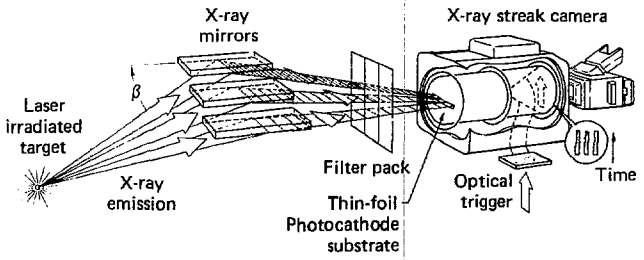

Figure 16. Three-channel reflector-filter operation schematic. X rays are emitted from the laser fusion target and are filtered by the x-ray mirrors, the absorption-edge filters, and the photocathode substrate.

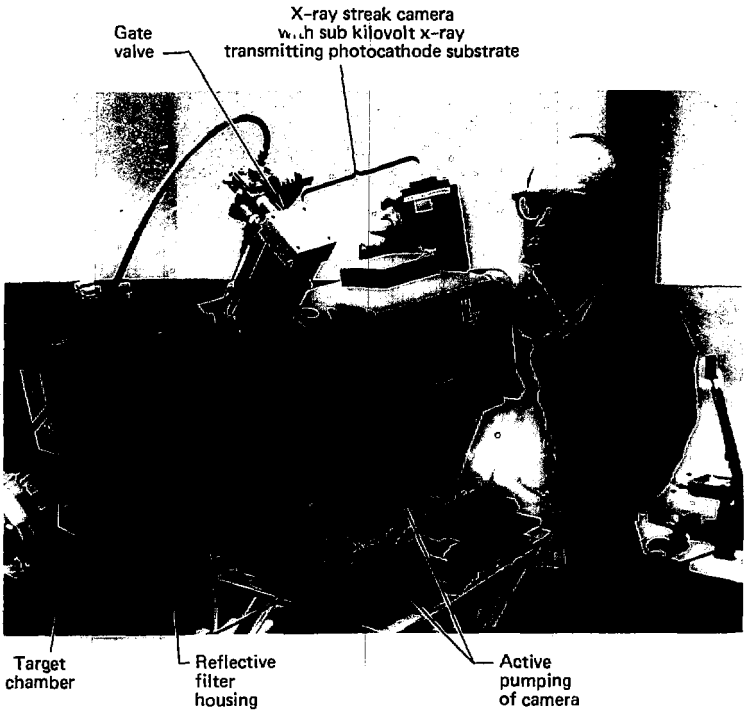

Figure 17. The SXRSC with the x-ray mirror housing.

Chapter 4

CALIBRATION AND EXPERIMENTS

The SXRSC was tested to determine its basic operating characteristics and capabilities. Calibration and basic experimental work was performed on the Monojoule laser. The overall system sensitivity was then modified for high-power target irradiation experiments conducted at the Argus laser facility at LLNL. This chapter describes the apparatus and the proceedures involved in the calibrations. Time-resolved measurements of gold-disk x-ray emissions are also presented and discussed.

Monojoule Laser Facility

The Monojoule laser is a neodymium:YAG laser capable of producing single laser pulses with energies between one and three joules and 50-psec to 150-psec pulse widths. The calibrations reported here used 1-J, 150-psec laser pulses. The laser operates with a passively mode-locked oscillator. Mode-locking is done with a saturable absorber. A 150-psec, 1-mJ pulse is switched out of the peak of the oscillator wave train with a spark gap. The oscillator pulse passes through two 3/8-inch YAG preamplifiers, a 5/8-inch glass amplifier and a one-inch glass amplifier as shown in figure 18. This amplification process raises the pulse energy to one joule.

For x-ray streak camera calibration the laser pulse is directed through an étalon to produce a series of optical pulses,

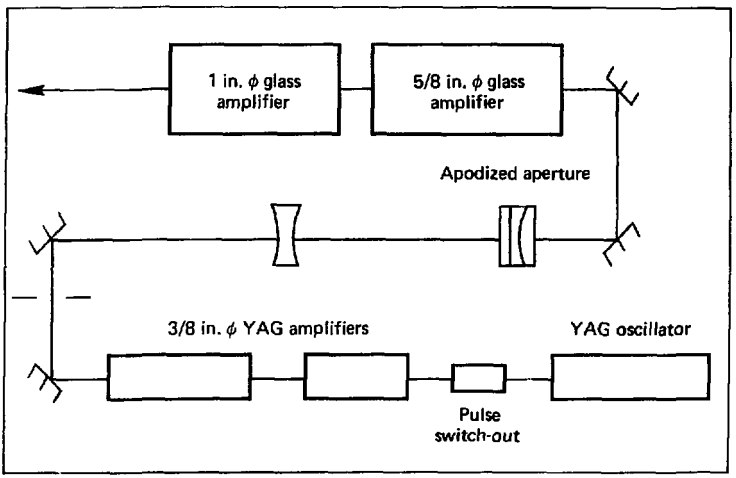

Figure 18. The Monojoule laser, a 150-psec one-Joule neodymium:YAG laser used for diagnostic testing and development.

typically 500 psec apart, each pulse having one-half the energy of the preceding pulse. X-ray pulse trains are produced by irradiating an iron slab target with the laser pulse train in an evacuated (10^{-5} Torr) target chamber. In full-power operation the Monojoule laser can operate with a three-minute repetition period for efficient calibration and testing procedures.

Experimental Configuration

A schematic of the experimental configuration is shown in figure 19. For calibration the SXRSC is positioned on the target chamber at forty-five degrees to the incident laser beam. The target-to-cathode distance is 36 cm without the x-ray mirror housing and 52 cm with the mirror housing in place. Triggering of the SXRSC is accomplished by diverting part of the oscillator pulse directly to a photodiode. The photodiode generates an electrical pulse which triggers the streak camera's avalanche-transistor sweep circuit. Path length traveled by the optical/electrical pulse controls the trigger timing relative to the incident x-ray pulse train.

Temporal Calibration

The soft x-ray streak camera temporal calibration procedure consists of recording a string of x-ray pulses with known temporal spacing and relative energies. The resultant streak camera data are then routinely reduced and analyzed to show sweep speed, sweep linearity, dynamic range, and photocathode uniformity. Figure 20 is the photographic record of an x-ray pulse train. These data were

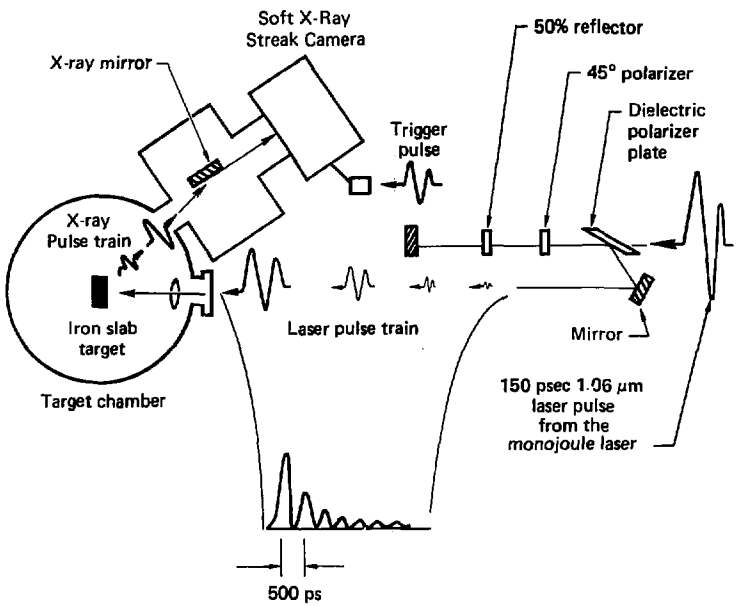

Figure 19. The Monojoule target chamber calibration and experimental configuration. A 500-psec etalon splits the 1.06-μm laser pulse into a pulse train which heats the iron slab target and produces a train of x-ray pulses. The x-ray pulse train is reflected by an x-ray mirror onto the streak camera slit.

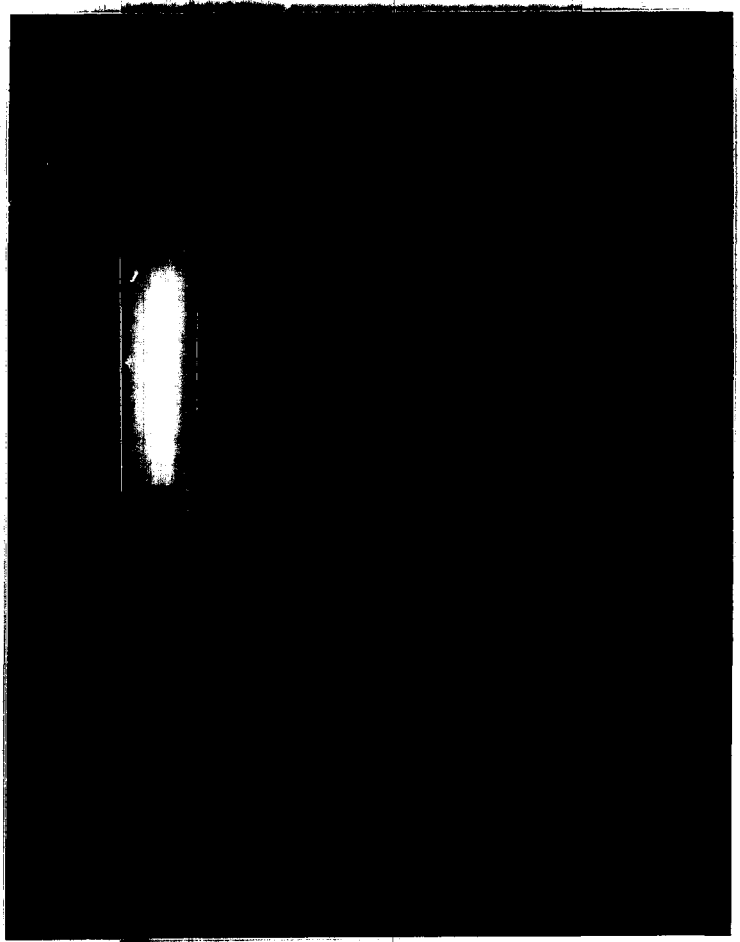

Figure 20. Soft x-ray streak camera calibration data. The streaked x-ray pulse train image is exposed on the center of the Kodak Royal-X Pan film. A step wedge is exposed on the edge of each film to permit a density-versus-intensity reduction of the recorded data.

taken without reflective or absorptive filtering, other than that of the carbon photocathode substrate.

Data Reduction

The data are taken on Kodak Royal-X Pan film for maximum sensitivity and resolution. After the data are recorded and before the film are developed, a strip at the edge of the film is exposed to a stepwedge which is chromatically matched to the image intensifier phosphor (Fig. 20). The film is then developed for 4.5 minutes in Kodak DK-50 developer. This development procedure raises the film speed to ASA 2000 and lowers the contrast of the film to allow a large dynamic range to be recorded. Intensity-versus-position is extracted using a computer-controlled microdensitometer. The stepwedge data are interpolated using a polynomial fit to produce a D-logE calibration curve characteristic of both the particular development and piece of film (Fig. 21). The density data are then unfolded with the D-logE curve to produce intensity-versus-position information (Fig. 22).

The spatial separation of intensity peaks divided by the étalon-controlled temporal separation of the pulses (500 psec) shows the camera's inverse sweep speed with a X3 sweep card to be 134 psec/mm. Sweep linearity is easily deduced from comparison of the pulse separations along the pulse train.

Dynamic range[1] is a function of resolution, pulse width, and other camera operating parameters. For the temporal resolutions of

[1]S. W. Thomas and G. E. Phillips, in Proceedings of the 13th International Congress on High Speed Photography and Photonics, edited by Shin-ichi Hyodo (Japan Society of Precision Engineering, Tokyo, Japan, 1979), pp. 471-475.

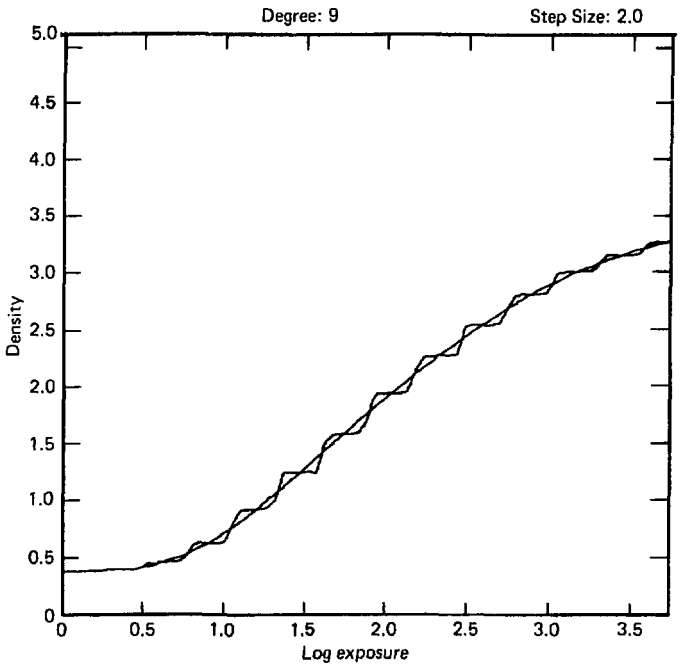

Figure 21. D-LogE characteristic curve of the film, a 9-degree polynomial fit to stepwedge data.

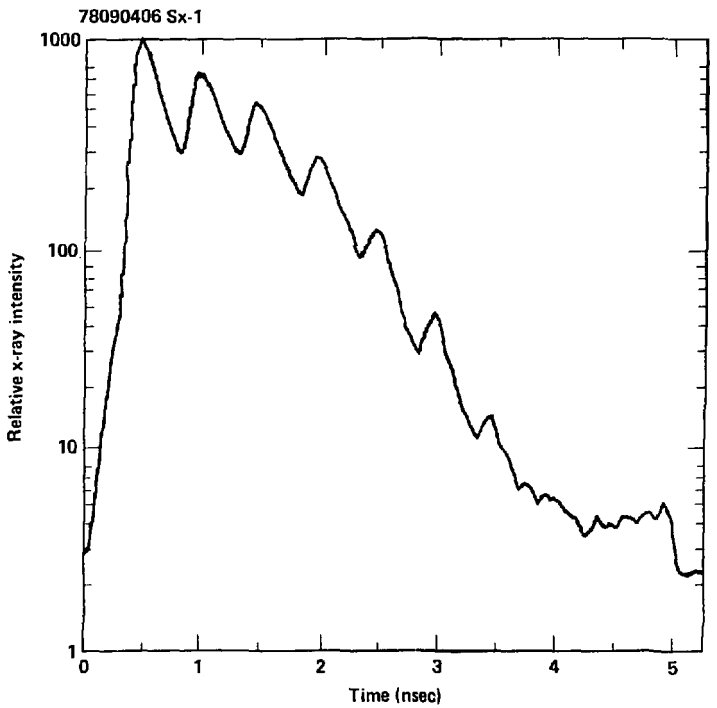

Figure 22. Streaked intensity-versus-time of an x-ray pulse train.

interest here, a dynamic range of greater than one thousand is not unusual and will be evident in the data presented. Full saturation was not seen with laser-pulse energies on target as high as 800 mJ. X-ray pulses generated by laser energies as low as 4 mJ were easily discernible above the noise level.

The 50-$\mu g/cm^2$ carbon substrate with a 300-Å gold photocathode was seen to be extremely uniform across the slit. Figure 23 is the cathode response-versus-slit position information taken from the data shown in figure 20.

5-Degree Carbon Mirror Tests

Preliminary tests were done with a 5° carbon x-ray reflector. A filter pack was positioned in front of the 50-$\mu g/cm^2$ substrate to produce four channels, #1 with no filtering, #2, #3, and #4 with filters of 100-$\mu g/cm^2$, 200-$\mu g/cm^2$, and 300-$\mu g/cm^2$ of carbon respectively. The calculated channel response is given in figure 24. Data from a one-joule shot are shown in figures 25 and 26. The calculated response shows expected relative channel intensities of approximately 1, 0.5, 0.2, and 0.1 for channels #1 through #4. The measured relative intensities were 1, 0.5, 0.3, and 0.1, which is well within the error of the calculated estimate.

A test was also performed to crudely check the high-energy cutoff property of the x-ray reflector. The x-ray flux from a one-joule target shot reflected from the five-degree carbon mirror was measured both with and without an 8-μm-thick beryllium filter. Because this filter has strong absorption below 1 keV, its combination with the reflector should and did absorb all signal, giving a null

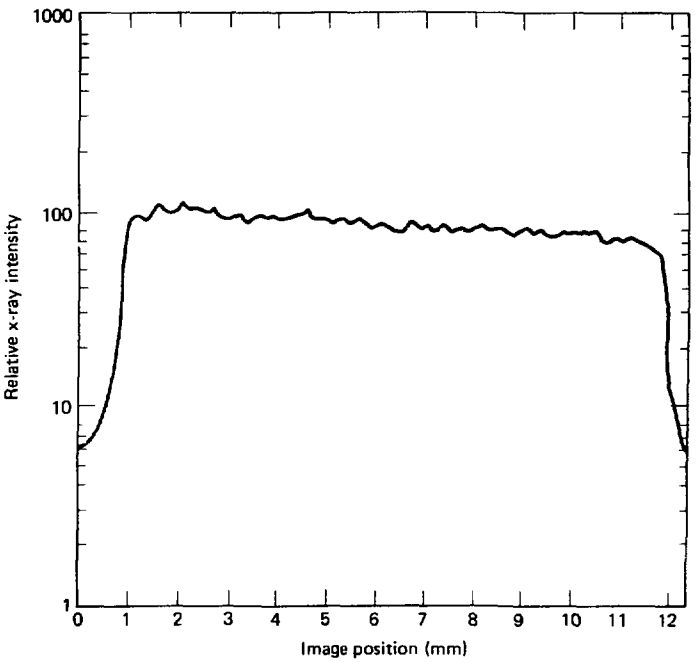

Figure 23. An intensity-versus-position scan across the photocathode slit of SXRSC calibration shot data showing the uniformity of the photocathode and the photocathode substrate.

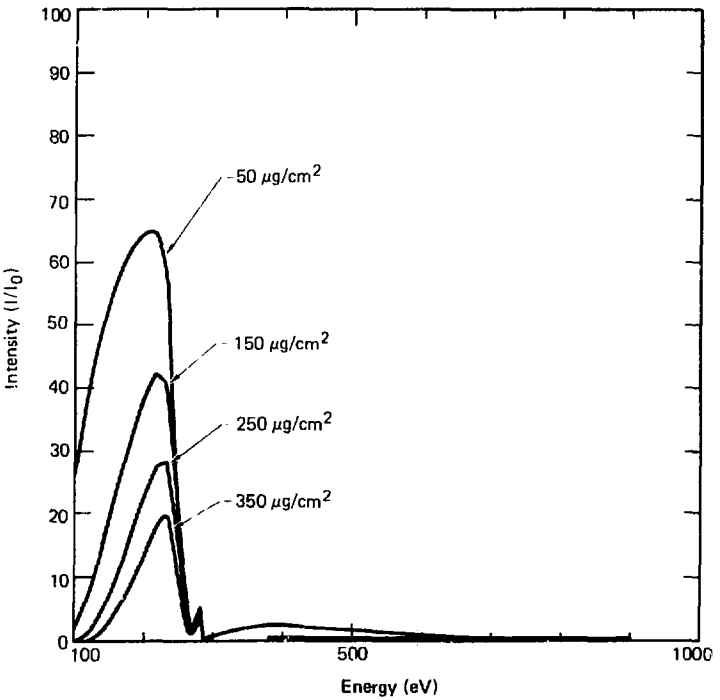

Figure 21. Calculated responses of a 5° carbon reflector with four absorber channels: 50-$\mu g/cm^2$, 150-$\mu g/cm^2$, 250-$\mu g/cm^2$, and 350 $\mu g/cm^2$ thick carbon filters (including the 50-$\mu g/cm^2$ carbon photocathode substrate).

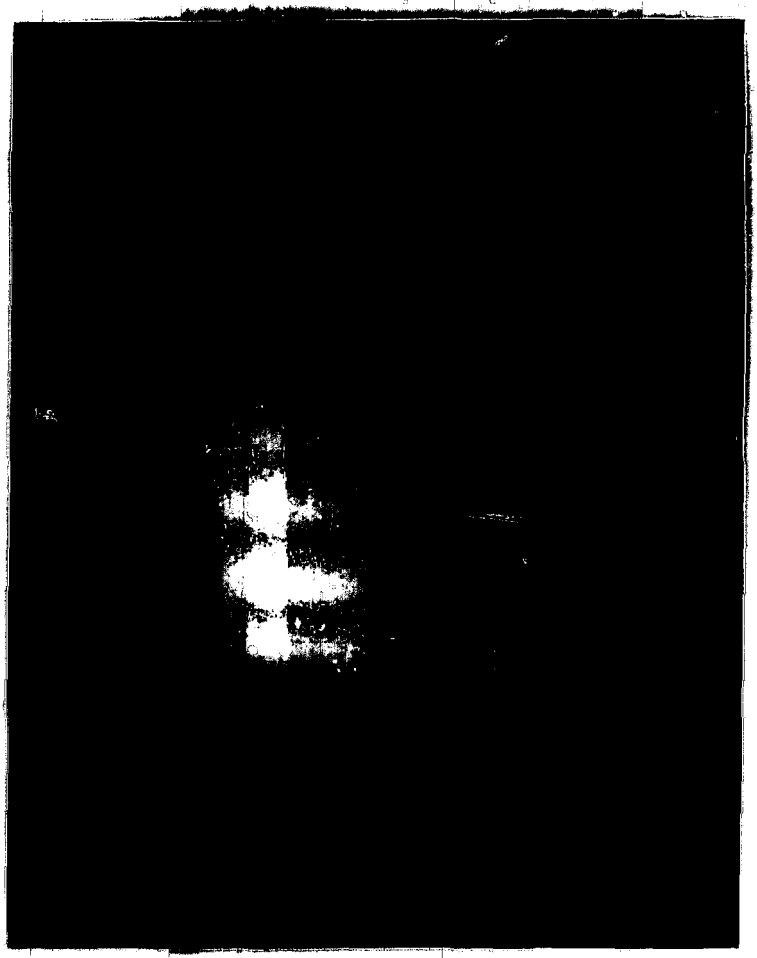

Figure 25. SXRSC streak data of four carbon channels.

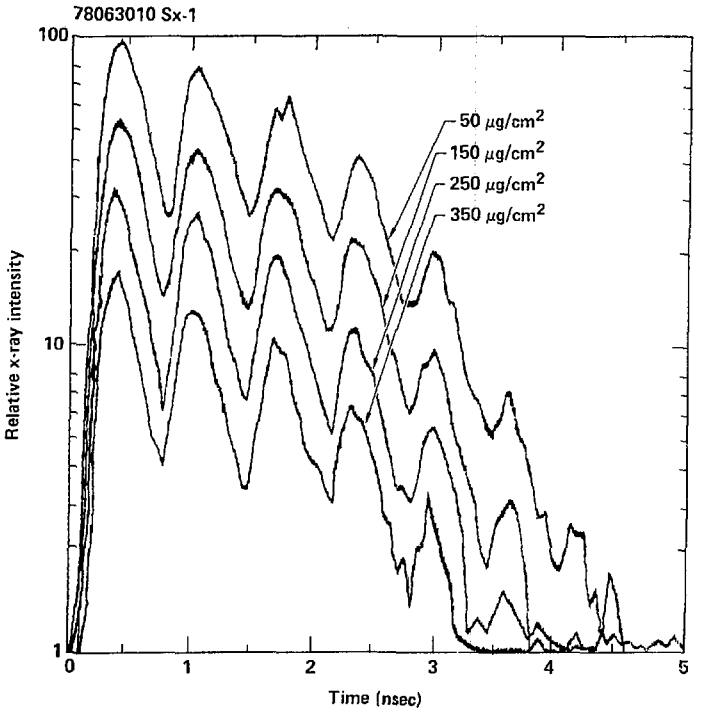

Figure 26. Intensity-versus-time scan of the streak data from the four carbon channel experiment. The ratio of intensities between channel #1, which was unfiltered except for the 50-$\mu g/cm^2$ carbon substrate, and channels #2, #3, and #4 were 0.5, 0.3, and 0.1 *respectively*.

shot. Strong signals from similar target illuminations with this filter, but without an x-ray reflector, verify that suprakilovolt x rays are indeed absorbed by the mirror.

Stepped Photocathode Experiments

An experiment[2] was performed to empirically measure the relative responses of different photocathode thicknesses and to determine the optimum photocathode thickness. A photocathode was built with thickness increasing across the slit length in a series of steps. This photocathode consisted of six thicknesses of gold vacuum deposited on a 50-$\mu g/cm^2$ carbon substrate. The steps were measured interferometrically to be 130 Å, 340 Å, 550 Å, 800 Å, 1100 Å, and 3200 Å thick, with a measurement uncertainty of 30 Å. This stepped photocathode was irradiated with a pulse train of subkilovolt x rays from an iron target at the Monojoule laser. The shot data are shown in figure 27. The most sensitive channel is the 130-Å-thick section. From the discussion of transmission properties in chapter 2, this indicates that the secondary electron range in gold is ~130 Å. The narrow bright streaks between the photocathode channels are regions which were partially masked during the evaporation deposition of the gold steps.

The average intensity of each channel as a function of time is given in figure 28. There is no apparent degradation of the photocathode temporal response with increasing thickness. The gold photocathode sensitivity can be seen to be a decreasing function of

[2]G. L. Stradling, H. Medecki, R. L. Kauffman, and D. T. Attwood, Appl. Phys. Lett., Vol. 37, 782(1980).

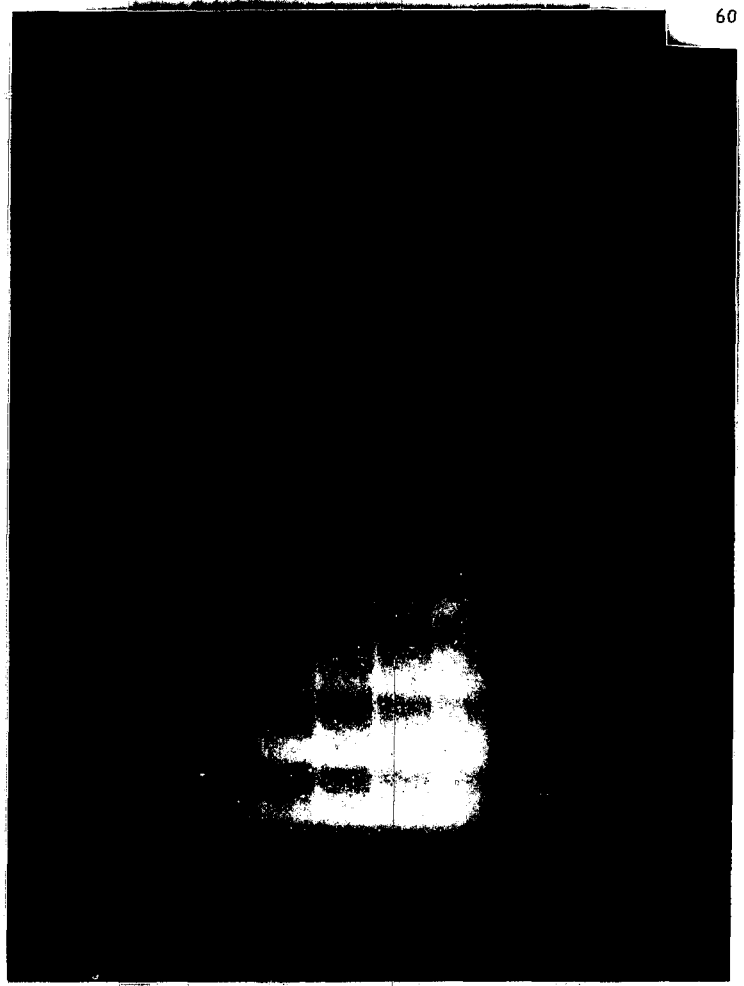

Figure 27. Streak data from a stepped-photocathode calibration shot.

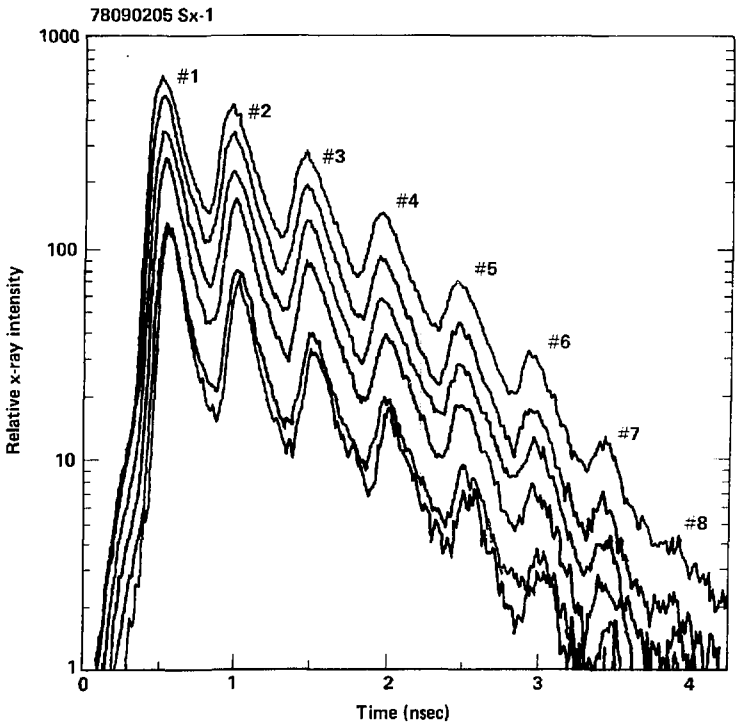

Figure 28. Relative intensity-versus-time plot of six stepped photocathode channels over eight successive x-ray pulses.

thickness for thicknesses greater than 130 Å. The sensitivity of the 3200-Å channel is a factor of six lower than that of the 130-Å channel.

High-Power Applications

The calibration shots showed the SXRSC to be very sensitive. Light pulses on target with energies of 800 mJ produced signals which approached saturation. The primary use of the SXRSC will be to diagnose experiments performed the Argus laser facility, which operates with energies on target of order one kilojoule. Clearly the camera's sensitivity must be decreased by a factor of 10^3 to 10^4 to allow the SXRSC to function as a diagnostic on kilojoule target shots.

Sensitivity Reduction Techniques

Several methods are available to avoid camera saturation during high-energy target shots. The target x-ray signal can be decreased by positioning the camera farther from the source. This provides a decrease in signal proportional to r^{-2}. The signal can be further attenuated using thicker absorption-edge filters. The x-ray photocathode response to the x-ray signal can also be varied by changing the photocathode volume. In addition, the image intensifier gain can be decreased or the film speed can be reduced.

The first three options are best because they avoid excessive electron-flux levels[3] in the image converter tube. High electron

[3]R. Kalibjain, in Proceedings of the 13th International Congress on High Speed Photography and Photonics, edited by Shin-Ichi Hyodo (Japan Society of Precision Engineering, Tokyo, Japan, 1979), pp. 452-455.

fluxes in the image converter tube result in space-charge repulsion effects and an accompanying decrease in signal-gain linearity.

A reduction of x-ray flux levels for high-power laser shots is accomplished by physically positioning the SXRSC three meters from the Argus target. This decreases the x-ray flux by a factor of about thirty below that detected at the 52-cm calibration distance. Figure 29 shows the SXRSC mounted on the Argus target chamber at the end of a three-meter flight tube. Filter thicknesses for the reflector-filter combinations were selected to bring the integrated responses of the three subkilovolt channels uniformly down by an additional factor of ten from the unfiltered response, for a total reduction of 300 due to these two items. The filters selected were 400-$\mu g/cm^2$ carbon, 500-$\mu g/cm^2$ vanadium, and 700-$\mu g/cm^2$ iron.

The photocathode response is a function of photocathode volume. The total x-ray deposition in the photocathode is proportional to the photocathode area and depends strongly on the photocathode thickness. Thus a factor of four reduction in photocathode response can be obtained by decreasing the photocathode slit width from 100 μm to 25 μm, raising the overall reduction factor to 1200. A slit of this width has been produced by an electron-discharge machining (EDM) technique, and is currently being used on kilojoule experiments at the Argus laser. The instrument sensitivity can be controlled within an additional factor of six by varying the gold photocathode thickness between 100 Å and 3000 Å. This allows a total signal reduction on the Argus facility of up to ~7000 in this geometry.

Figure 29. The SXRSC mounted three meters from the target on the Argus target chamber.

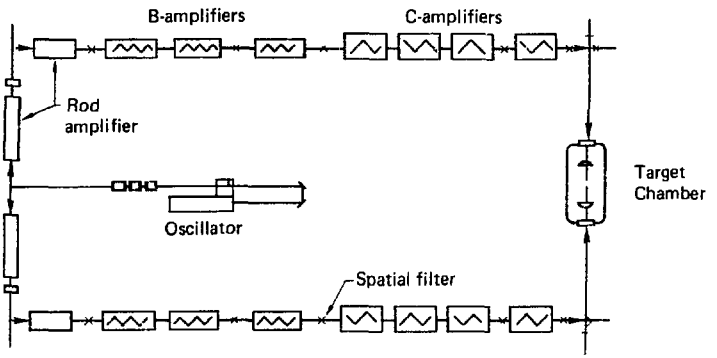

Figure 30. The Argus laser, a neodymium:YAG laser capable of producing kilojoule 1.06-μm pulses with pulse widths between 100 psec and 1000 psec.

The Argus Laser

The Argus laser is an advanced neodymium YAG laser which is capable of delivering more than 2 TW on target. The laser pulse is switched out of the oscillator, split, and sent through two chains of amplifiers (Fig. 30). The output beam from the last amplifier is 28 cm in diameter and has a peak flux of 5 J/cm^2. The energy-limiting factor of beam self-focusing is moderated considerably by high-vacuum spatial filtering and beam relaying techniques to eliminate hot spots across the beam.

Argus Gold-Disk Shot Data

Figures 31 and 32 show data obtained with a single-arm Argus shot onto a gold-disk target. The 400-psec laser pulse had an energy of 500 joules. The full three-reflector three-filter channels were in operation. The x rays in the 620-eV channel showed a 520-psec full width at half-maximum (FWHM), only slightly longer than the laser pulse. As might be expected from semi-equilibrium cooling of a radiating plasma, the lower-energy x rays were emitted for longer times. The 460-eV channel had a FWHM of 600 psec. The 220-eV channel had a 710-psec FWHM. In addition to providing temporally well-resolved data, intensities on these first shots were well within desired flux levels for this instrument, having been reduced by use of a 3-meter flight tube, absorption edge filters, a four-times-narrower photocathode slit, and a 300-Å photocathode.

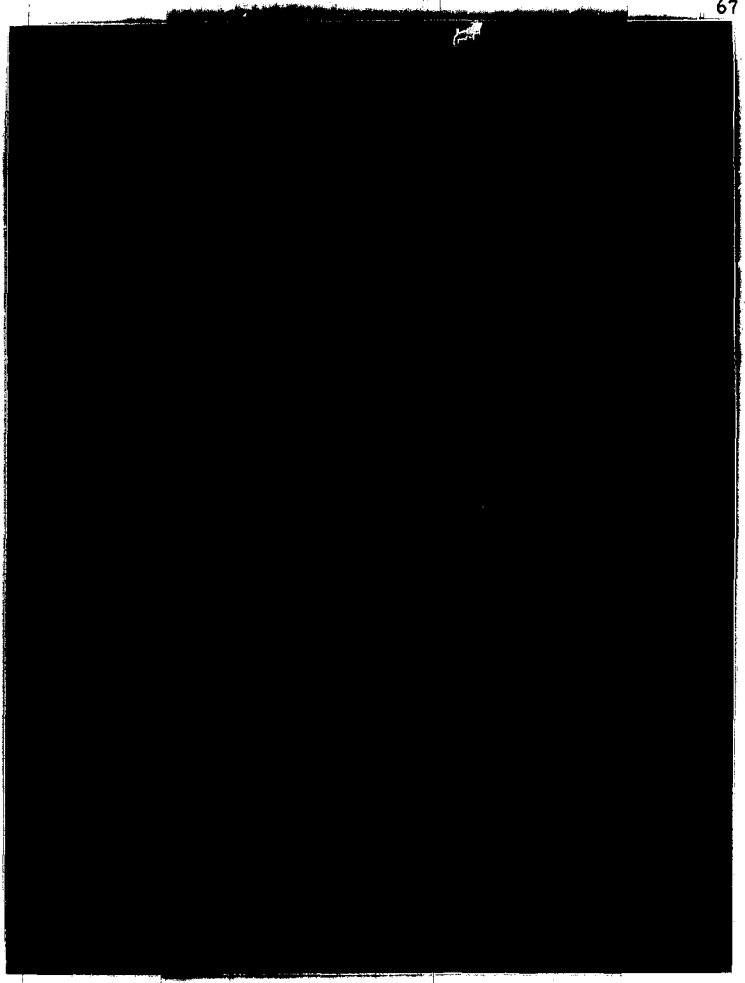

Figure 31. SXRSC temporally streaked x-ray image of an Argus gold-disk target shot with three reflector-filter channels.

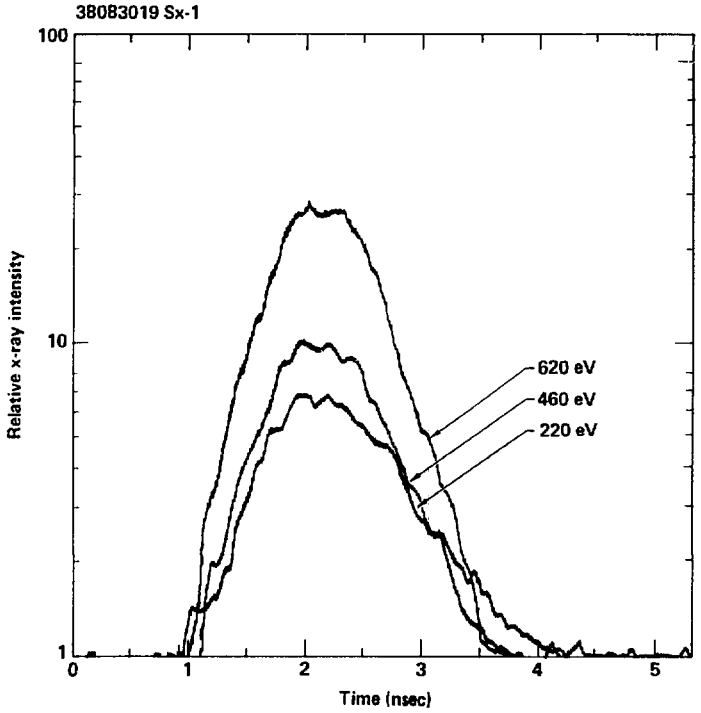

Figure 32. Intensity-versus-time data of three channels from an Argus gold-disk target shot. The three channel amplitudes are not normalized to each other in this illustration.

Chapter 5

FUTURE WORK AND SUMMARY

The soft x-ray streak camera will require additional research and calibration efforts to maximize its usefulness. There are also interesting problems dealing with streak camera technology that this instrument is well suited to investigate.

Future Work

An important part of SXRSC calibration still remains. The camera needs to be calibrated to determine absolute sensitivity, or signal-in to intensity-out gain. The reflector-filter response curves need to be determined empirically, particularly around the absorption edges where theoretical calculations are unreliable. More work needs to be done on optimization of present spectral channels, and development of more channels for better spectral definition. This calibration will increase the usefulness of the instrument in characterizing laser irradiated targets.

There are a number of applications of the SXRSC which are currently interesting. The spatial dimension across the photocathode slit can be used for one-dimensional imaging, as with an x-ray pinhole camera, or with an x-ray microscope. Time-resolved x-ray plasma spectroscopy can be done using various broadband or high-resolution soft x-ray dispersive devices.

In addition, the SXRSC is ideally suited for further investigation of the photocathode and image converter tube aspects of x-ray streak camera technology. When in the calibration mode on the Monojoule target chamber, photocathodes may be used, removed, examined, and replaced in a normal work day. The effects of substrates on photocathode performance can be investigated in detail. New photocathode materials now under study can be conveniently tested and compared with conventional photocathodes in pulsed operation in the streak camera environment. The vacuum pumping and internal pressure-measuring capabilities of the SXRSC will allow study of internal image converter tube problems and limitations.

Summary

The soft x-ray streak camera is a valuable, absolutely necessary addition to the laser fusion diagnostic capability. As a time-resolved spectrometer, it provides new information to aid the understanding of energy transport in laser fusion targets. This instrument is sensitive to photon energies down to 100 eV. It has been calibrated for sweep speed, dynamic range, and linearity. The SXRSC has 15-psec temporal resolution and a dynamic range greater than 1000.

The extremely uniform one-dimensional photocathode has been used with multiple reflector-filter pairs to produce three narrow channels spanning the 100-eV to 700-eV spectral region. An easily removable cathode assembly has allowed preliminary study of photocathode characteristics. Measurements have been made which indicate a peak gold photocathode response for a thickness of ~130 Å.

The SXRSC has been sucessfully used on high-power Argus experiments to show temporal pulse widths for three subkilovolt energy channels at 220 eV, 460 eV, and at 620 eV, and is now used as a routine diagnostic instrument.

ACKNOWLEDGMENTS

The author acknowledges the assistance of his advisor Larry V. Knight. He also gratefully acknowledges the assistance and direction generously provided by David T. Attwood, whose support made this project possible.

The author is indebted for the many beneficial conversations with N. M. Ceglio, S. W. Thomas, R. L. Kalibjian, A. Tour and R. L. Kauffman. He would also like to express his appreciation for the technical assistance received from J. W. Houghton, D. P. Gaines, C. L. Athey, E. L. Pierce, W. R. McLerran, G. E. Phillips, and C. H. Dittmore

A SOFT X-RAY STREAK CAMERA FOR LASER FUSION APPLICATIONS

Gary L. Stradling

Department of Physics and Astronomy

M.S. Degree, April 1981

ABSTRACT

This thesis reviews the development and significance of the soft x-ray streak camera (SXRSC) in the context of inertial confinement fusion energy development. A brief introduction of laser fusion and laser fusion diagnostics is presented. The need for a soft x-ray streak camera as a laser fusion diagnostic is shown. Basic x-ray streak camera characteristics, design, and operation are reviewed. The SXRSC design criteria, the requirement for a subkilovolt x-ray transmitting window, and the resulting camera design are explained. Theory and design of reflector-filter pair combinations for three subkilovolt channels centered at 220 eV, 460 eV, and 620 eV are also presented. Calibration experiments are explained and data showing a dynamic range of 1000 and a sweep speed of 134 psec/mm are presented. Sensitivity modifications to the soft x-ray streak camera for a high-power target shot are described. A preliminary investigation, using a stepped cathode, of the thickness dependence of the gold photocathode response is discussed. Data from a typical Argus laser gold-disk target experiment are shown.

COMMITTEE APPROVAL:

Larry V. Knight, Committee Chairman

James M. Thorne, Committee Member

Clark. G. Christensen, Graduate Coordinator